View Article Online
View Journal

Environmental Science Nano

Accepted Manuscript

This article can be cited before page numbers have been issued, to do this please use: J. Subbotina, O. McElligott and V. Lobaskin, *Environ. Sci.: Nano*, 2026, DOI: 10.1039/D5EN00784D.

ROYAL SOCIETY OF CHEMISTRY

rsc.li/es-nano

View Article Online
DOI: 10.1039/D5EN00784D

Micro- and nanoplastics are significant environmental pollutants with increasing human exposure. While chemically inert, these particles pose potential health risks through environmental modifications and as carriers of toxic substances. Understanding nanoplastic surface properties' influence on bionano interactions and particle circulation is crucial. Limited information exists on plastic-biomolecule interactions due to polymer variability and diverse physicochemical characteristics of degraded particles, while experimental research costs create barriers. To advance nanosafety assessment of polymeric nanomaterial-protein interactions, we extended previously reported CoronaKMC/UnitedAtom coarse-grained approach for modeling polymeric materials. This extension focuses on physics-based parameterization of protein-nanoparticle interfaces for noncrystalline polymers, particularly polystyrenes. Reported computational approach predicts protein corona compositions for polystyrene nanotoxicity and protein orientations on nanoparticles, modeling biomolecular adsorption based on bio-nano interface parameters. It can be used as a "Safe and Sustainable by Design" (SSbD) nanoinformatics toolkit for designing safer polymers.

View Article Online
DOI: 10.1039/D5EN00784D

Journal Name

ARTICLE TYPE

Cite this: DOI: 00.0000/xxxxxxxxxx

Modelling bionano interactions and potential health risks for environmental nanoplastics: the case of functionalized polystyrene.†

Julia Subbotina,*[a] Oran McElligott,[a] and Vladimir Lobaskin[a]

Received Date
Accepted Date

DOI: 00.0000/xxxxxxxxxx

Micro- and nanoplastic pollution has been raising increasing concern due to their adverse environmental and potential human health effects. The impact of plastic particulates, especially in their nanoforms, on the health of living organisms is not fully understood. Based on substantial evidence, it can be assumed that the key processes underlying the bioaccumulation and toxicity of nano-sized materials are controlled by bio-nano interactions, particularly through the formation of protein coronas. Understanding the composition of such biocoronas and the factors governing their formation can aid in material risk assessment and the development of safety measures. In this study, we report on novel parametrization of *UA/CoronaKMC* coarse-grained multiscale approach for predicting protein corona composition that can be formed on pristine (PS) and modified forms (PS-NH_2 and PS-COOH) of polystyrene nanoplastics in blood plasma. Reported methodology extends the use of *UA/CoronaKMC* method for further implementations into digital machine-learning SSbD frameworks for pre-assessments of the nanotoxicity of novel polymers.

1 Introduction

To date, numerous polymeric materials have been introduced to the global market, and polystyrene (PS) consistently represents about 5% of the total annual global polymer production by volume[1]. They offer significant advantages by providing cost-effective solutions for the production of various consumable goods. However, the increase in polymeric consumables combined with the inadequate waste management (note that global recycling rates are low 9%[2]), leads to the accumulation of enormous volumes of polymer waste in landfills and aquatic environments at the end of their life cycle[2–5]. Without proper recycling practices, plastic waste degrades under exposure to environmental conditions initially to microparticles (microplastic) and subsequently to nanoparticles (nanoplastic)[6]. This process can be relatively fast, e.g., it might take less than two months to reach the nanoparticle (NP) state with sizes smaller than 250 nm for disposable PS-made coffee lids[7]. The environmental spread of nanoplastics is undeniable. Their presence was recorded in aquatic ecosystems[8,9], in the atmosphere[10], and in the soil[11,12]. It was even observed in the ice samples obtained from the remote Arctic and Antarctic regions[13,14]. As a result of this widespread pollution, nanoplastics penetrate into human body through various pathways: food (oral ingestion), water (absorption by the skin or oral ingestion), or the air (inhalation)[15–17]. Plastics, detected in human faeces[18], in human placenta (referred to as "plasticenta")[19], or in the brains of humans and other mammals[20,21] point to the alarming scale of this exposure.

A concerning consequence of nanoplastic pollution is caused by environmental degradation of polymers that produces not only different particle sizes but also numerous variations of surface chemistry, as a result of physical processes and reactions with chemicals co-located with polymeric waste[22–30]. Surface modifications enhance the colloidal stability of the nanoplastics and can transform a relatively inert polymer bulk material into a distribution of "activated" NPs. Surface-modified NPs can be internalized by living organisms and pass through the blood-brain barrier (BBB) in a manner similar to more reactive inorganic NPs[31–37].

The primary factor facilitating this process is the adsorption of proteins onto the hydrophobic surface of the NP as it enters the bloodstream. Exogenous agents are typically encountered by opsonins, such as antibodies or complement proteins, which bind to these agents, marking them for destruction by phagocytes and facilitating their clearance. However, during this process, opsonins compete with other blood proteins, and the ultimate composition of the protein layer on the NP's surface, known as the protein "corona", will determine the fate of the NPs[38–41]. This protein makeup, especially if enriched with dysopsonins, gives the NP a "new identity' that can help avoid the recognition process

[a] School of Physics, College of Science, University College Dublin, Dublin 4, Ireland. E-mail: yulia.subbotina@ucd.ie

† Supplementary Information available: [details of any supplementary information available should be included here]. See DOI: 00.0000/00000000.

View Article Online
DOI: 10.1039/D5EN00784D

by mononuclear phagocyte system (MPS)[42,43]. As a result, this competition may help NP remain undetected by MPS for longer, increasing its blood circulation times and its persistence[44].

The impact of nanoplastic pollution on various living organisms has been extensively examined in the recent literature[45–51]. Specifically, with regard to PS, research has demonstrated that its nanotoxicity can differ between organisms[52]. In humans[53], particular emphasis was placed on the health of women and fetal development during pregnancy[54–57]. Moreover, research has consistently demonstrated a robust correlation between metabolic disorders and exposure to PS NPs in both animal models and cellular systems[58–63].

PS NPs have also been increasingly noted for their neurotoxic effects. There is increasing evidence from animal studies on the negative role of PS NP exposure to anxiety, depression, cognitive impairment, and neurodevelopmental disorders both in adults and after developmental or maternal exposure[64–68]. The exposure time of PS NP was shown to be irrelevant for health outcomes, as short-term exposure was associated with long-term cognitive decline, neuronal damage, and inflammation[69]. PS NPs, specifically anionic ones, may exacerbate Parkinson's disease pathology by disrupting the gut–brain axis, facilitating α-synuclein aggregation, and inducing neuroinflammation and mitochondrial dysfunction[70–75].

Understanding the factors governing nanotoxicity is crucial for predictive environmental toxicology as well as for developing safe biomedical applications based on PS NPs. The protein corona composition was shown to be a crucial determinant of nanotoxicity[76–78]. It shapes how NPs interact with cells and organs, and ultimately modulates NP's toxicity and immune responses. At the same time, protein corona composition is an imprint of NP characterised by a set of intrinsic (material type, surface chemistry, size) and extrinsic (zeta potential, colloidal stability, and solubility) properties that are affected by the specific environments (chemical compositions, pH, ionic strength)[79–81]. Manipulation of the intrinsic and extrinsic properties of NPs experimentally can help identify safer materials that degrade to NPs with the preferred corona composition. However, experimental assessments of many combinations of protein corona-NP systems might be a tedious task. Recent advances in modelling the protein corona facilitate the rational design of safer nanomaterials. These methodologies, ranging from multiscale physics-based modelling[82–86] to machine-learning approaches[39,87–89], are revolutionising the material design and safety assessment.

In our previous work, we introduced and applied a multiscale *United Atom* (*UA*) method combined with *a Kinetic Monte Carlo* approach to model protein corona compositions (*CoronaKMC*) and predict the nanotoxicity of crystalline materials with varying complexities as a function of the composition of the protein corona[90–94]. In this study, we extend this methodology to include a polymeric material, PS. Our multiscale simulations are designed to model key molecular events of individual and collective protein-NP interactions by examining protein adsorption and biocorona formation on functionalized PS NPs with different charges. The adsorption of the five most prevalent proteins in blood plasma, namely serum albumin (HSA), fibrinogen (FG), immunoglobulin IgG (IGH), complement component 3 (C3), and apolipoprotein A1 (APO-AI), onto small, 10-nm PS NPs is taken into account. The new *UA* parameters for coarse-grain (CG) modelling of protein-PS NPs are developed. The results of the CG simulations are compared with existing experimental data and higher-resolution computational simulations. The novel parameterisation expands the capacity of *UA/CoronaKMC* for modelling common industrial materials. The results obtained are then used to assess the potential biomedical application of PS NPs.

2 Methods

We first introduce the protocol for building a CG model of PS surfaces. Modified PS NPs will be designed as decorated raspberry core-shell CG structures originally described in[93] to mimic the roughness of weathered materials. The CG mapping for proteins is set at one bead per amino acid (AA) resolution (see subsection 2.1), while each PS bead represents a styrene tetramer. The parameterisation protocol for obtaining CG interaction potentials for the novel *UA* beads used in constructing the raspberry models is described in Section 2.4.3. Protein corona formation (subsection 2.2) is modelled using a combination of the *UA* method with kinetic Monte Carlo (KMC) simulations[91,94,95].

2.1 General concepts of the multiscale model for predicting individual protein adsorption affinities.

In this work, we use the *UA* model to evaluate the average protein adsorption energy, as described in our previous publications[90,92–99]. In this model, the complete protein- interaction potential U_{p-NP} is approximated by a sum of non-bonded pairwise-additive interaction terms for each AA in the protein and the NP modelled as a set of CG beads with assigned *UA* material-specific parameters:

$$U_{p-NP} = \sum_{i=1}^{N_{AA}} U_i(d_i(\theta,\phi)) = \sum_{i=1}^{N_{AA}} U_i^{el}(d_i(\theta,\phi)) + \\ + \sum_{i=1}^{N_{AA}} U_i^{s}(d_i(\theta,\phi)) + \sum_{i=1}^{N_{AA}} U_i^{c}(d_i(\theta,\phi)) \quad (1)$$

Here, the AA-specific non-bonded interaction potentials near the material surface U_i^s are obtained from all-atom molecular dynamics (MD) simulations in tabulated form (see *UA* material parameterisation protocol in Section 2.4.3) and include all types of non-bonded interactions modelled at this level of resolution. The long-range interaction potentials U_i^c implement van der Waals interaction between the remaining NP's region (core, labelled with "c") and AA, and are calculated from the optical properties of the core material and the AA by the Hamaker procedure[100]. The electrostatic interactions are described using screened Coulomb potentials[94]. The *UA* configurational files *.CONFIG containing dielectric parameters, ionic strength, *etc.*, employed in simulations, are provided in the supporting GitHub archive.

Within the *UA* paradigm, both materials constituting the bio-nano

View Article Online
DOI: 10.1039/D5EN00784D

interface – the protein and the NP – are modelled using a rigid-body approximation, i.e., we neglect any possible change of the protein conformation (no side-chain flexibility or backbone motion are allowed) or PS chains at the NP surface. Interfacial water at the bio-nano interface is included explicitly at short distances via the short-range surface potential and implicitly beyond the cut-off distance of the atomistic model and defined by the force field selected for MD simulation (see Section 2.4.3 for more information).

The potential U_{p-NP} depends on the position of the protein with respect to the NP surface and is determined by d_i, the distance between the NP surface and the protein surface (surface-surface distance or SSD) and by the orientation of the protein characterized by two rotational angles, θ and ϕ, relative to the initial orientation of the protein and the normal of the surface (z-axis). The angles θ and ϕ correspond to an initial vector in the reference frame of the protein, which is rotated so that this vector faces the surface of the NP when the centre of mass of the protein is in a position $(0,0,z)$ relative to the surface of the NP. The rotational transformation is sequential with the first rotation of the protein by $-\phi$ around the z-axis, followed by $180^\circ - \theta$ rotation around the y-axis. In a reference frame (at $[\phi,\theta]=[0^\circ,0^\circ]$), the protein is initially aligned to the principal axis with the longest axis along z and the second longest along the y-axis. The plot of adsorption energy values $E_{ads}(\phi,\theta)$, obtained by integrating the interaction potential along the z-axis in a given protein orientation in the θ,ϕ coordinate space,

$$E_{ads} = -k_B T \ln\left[\frac{\int_{R_{min}}^{R_{max}} \xi^2 e^{-U_{p-NP}/k_B T} d\xi}{\int_{R_{min}}^{R_{max}} \xi^2 d\xi}\right] \quad (2)$$

produces the adsorption energy surface (AES) map or a *heatmap*. The adsorption energy E_{ads}^{min} is the lowest energy obtained from AES and corresponds to the most stable complex of the protein adsorbed on the NP surface. Multiple comparably stable minima can be located in the protein adsorption heatmaps (see examples in Figure 1). By moving the protein along the z-axis and rotating through θ and ϕ angles from the initial orientation, the *UA* model samples the configurational ensemble. The total protein adsorption energy $\langle E_{ads}^{Boltz}\rangle$ is calculated by canonical Boltzmann averaging over all possible configurations[101]:

$$\langle E_{ads}^{Boltz}\rangle = \frac{\sum_i \sin\theta_i e^{-(E_{ads})_i/k_B T}(E_{ads})_i}{\sum_i \sin\theta_i e^{-(E_{ads})_i/k_B T}}. \quad (3)$$

2.2 CoronaKMC model of protein corona formation (competitive adsorption).

Competitive binding of blood plasma proteins during the corona formation is a multifaceted, dynamic process that takes place in two regions of the bio-nano interface[102]. It is accepted that the corona hierarchy is multilayered, yet the majority of published studies focus on monolayered coronas[103]. Proteins binding to the surface may do so irreversibly, resulting in the formation of a "hard" corona. In contrast, proteins that are weakly bound undergo reversible adsorption, remaining in a "soft" corona region until they are supplanted by incoming proteins with higher adsorption affinity. In addition, proteins from solution may bind to the adsorbed proteins of the "hard" corona, thus forming further adsorption layers[104]. Proteins in both categories compete for available binding sites on the NP surface, a phenomenon known as the Vroman effect. This competitive process persists until the system reaches equilibrium, at which point proteins with the highest individual binding energy saturate the adsorption sites. Protein concentration also influences this process: proteins present in higher concentrations are more likely to occupy the surface, whereas those arriving later and in lower concentrations can only fill the remaining gaps left by earlier arrivals. In case of relatively weak interactions between PS and proteins, the timescales of corona equilibration can reach hours and days due to the higher energy barriers related to the change of protein conformations that adopt their shape to have a stronger interaction with the surface as compared to the energy barrier for reversible desorption[105,106]. As a result, modelling the complete corona formation process with standard MD methods is practically unfeasible, although it has been attempted[75,107]. For example, in work[75] it took 75 ns of production run for human α-synuclein to make the initial contact with the PS surface, while the first signs of protein structural changes occurred after 400 ns of stimulation. To overcome the limits of corona dimensions and extreme timescales, we employ a KMC method[82,91,108–110], which proved to be more efficient in modelling adsorption/desorption events through the set of reaction rate equations for diffusion-driven collision events. However, that approach would miss the information on protein unfolding and the formation of further layers, which would require more detailed models of the proteins and their interactions[104].

Recently, we applied the hard-sphere (HS) KMC methodology[91,94] for predicting the formation of milk protein films on iron and aluminium surfaces[95,111]. The HS KMC method considers protein adsorption events as physical interactions between a patch of the protein and the NP surface. It also assumes that this process can be reversible. The attachment and detachment rates are calculated for different protein orientations chosen at random from the energy heatmaps, so proteins can bind to the NP surface on different sides; The method calculates the occupied NP surface fraction by calculating the projections of proteins as hard spheres with radius R_P corresponding to the radius of gyration of the molecule; The availability of binding sites on the NP surface for incoming protein is scaled according to the surface area occupied by other proteins.

A single event of protein adsorption is modelled as adsorption in random orientations. The probability of such a binding event is predicted from AES *UA* heatmaps. The latter are pre-calculated for individual proteins separately. In steady state and with the assumption that desorption is a first-order reaction and the adsorption is a pseudo-first-order, the rate constants for adsorption (k_a)/desorption (k_d) can be evaluated from the following equation:

$$\frac{k_a}{k_d} = K_{eq} = \exp\left(-\frac{\Delta G}{k_B T}\right) \quad (4)$$

View Article Online
DOI: 10.1039/D5EN00784D

Here, K_{eq} stands for the equilibrium constant, and the binding free energy ΔG can be represented by the protein adsorption energy in the given random orientation $E_{ads}(\phi,\theta)$ extracted from *UA* AES of individual protein:

$$\frac{k_a}{k_d} = e^{-E_{ads}(\phi,\theta)/k_BT} \tag{5}$$

The adsorption events between two entities, protein and NP, in solution are diffusion-controlled and occur with the collision rate k_s defined by Smoluchowski theory[112]:

$$k_s = 4\pi * (R_{NP} + R_P) N_A \frac{k_B T}{6\pi\eta} \left[\frac{1}{R_{NP}} + \frac{1}{R_p}\right] \tag{6}$$

where η is the viscosity of the medium and N_A is Avogadro's number. It is assumed that collision rates are diffusion-limited, the diffusion is isotropic, and hydrodynamic interactions are neglected. The per-site collision rate is then dependent on the surface available for adsorption and given by:

$$k_{coll} = \frac{1000 k_s A_p}{4\pi R_{NP}^2} \tag{7}$$

where A_p is the projected area and the factor of 1000 arises from the conversion from m^3 to L. The value of k_{coll} is taken as the adsorption rate constant with the condition that adsorption occurs with a unit probability after a collision event. Then, the desorption rate constant is:

$$k_d = e^{E_{ads}/k_BT} k_{coll} \tag{8}$$

This implies that a strongly negative adsorption energy results in a very low desorption rate. It should also be noted that E_{ads} is not the free energy of adsorption and is missing the entropic term. This approximation is only valid if entropy is small or constant across orientations.

2.3 CoronaKMC simulations setup and parameters.

In our HS KMC simulations, we employed rate constants and adsorption areas for each biomolecule orientation, which were obtained from the adsorbate parameters. This was accomplished by automatically converting .uam output and .pdb structures using the BuildCoronaParams script. This script takes a list of biomolecules and their concentrations in mol/L as input, locates the corresponding structures and .uam binding energy tables, and computes rate constants and adsorption areas for each biomolecule orientation. During the time-resolved KMC simulation, events are generated that correspond to the adsorption or desorption of adsorbates. Adsorption events involve choosing a potential adsorbate based on a probability proportional to its collision rate with the NP and generating a random position on the NP surface. Proteins were allowed to adsorb and be replaced during the evolution of the protein corona. As a result, only the final adsorbed protein fractions obtained after the system reaches equilibrium were considered to predict the corona composition. Time-dependent saturation of protein binding sites by all and individual proteins was used to monitor corona equilibration convergence. The KMC simulation time was set to 3 min for all three types of 10-nm PS NPs. The selected timescale was deemed sufficient to obtain converged protein corona compositions and was consistent with the experimental timescales reported for corona formation in PS NP[106,113,114] when the initial protein corona composition remained mostly unchanged from the moment of initial protein adsorption within 0.5 min frame.

To predict the corona composition, we applied realistic concentrations of the selected most abundant blood plasma proteins that were reported in the literature (see Table 2 for more information). A detailed description of the CoronaKMC model can be found in the original work[91,94].

2.4 Predicting individual protein adsorption affinities with the *UA* model.

To construct adsorption energy heatmaps for the KMC model and to estimate individual protein affinity to PS NPs, several steps must be executed. First, a raspberry model of unmodified or altered PS NPs with the Cartesian coordinates of NP raspberry beads should be developed. Second, *UA* parameters should be assigned to each NP raspberry bead. These parameters include the ζ potential, the Hamaker constant, charge, and radius. Third, Cartesian coordinates for proteins should be established. These coordinates can be obtained through experimental or computational methods. To ensure accurate AA content for *UA* calculations, it is necessary to evaluate the protonation state of the protein at the selected pH. Lastly, non-bonded pairwise U_i^s potentials should be provided in tabular format for every combination of NP raspberry bead and AA in the protein (potential mean force profiles or PMFs), including ionized AA states when necessary. If the *UA* distribution lacks potentials for specific material/AA combinations, they can be pre-calculated using all-atom MD simulations. The subsequent sections will provide comprehensive explanations on the implementation of these steps for novel parameterization of the *UA* model to characterize bio-nano interactions at PS interfaces.

2.4.1 Constructing CG models of functionalized PS NPs: surface morphology and Cartesian coordinates.

The raspberry model of NP and the corresponding Cartesian coordinates of the raspberry beads can be obtained with the help of *RaspberryGenerator.py* tool distributed with *UA* package. In the raspberry model, the volume of NP is discretized into many points (beads). The radii of these beads can vary, e.g., in our case, the NP is represented by a central bead of a uniform density with a set of smaller beads positioned at the outer layer. This approach was previously used for building modular CG models of core-shell polymer-coated NPs[93]. The coarse-graining algorithm was combined with Flory's theory[115,116] to obtain bead configurations corresponding to realistic shell density profiles of PEGylated NPs. The protocol reported in the current work was used to build CG models for PS NPs based on the following assumptions. While hydrophilic PEG chains can take various shapes at the NP interface (e.g., "mushrooms" or "brushes"), the morphology of the PS NP surface might be different due to less flexible

View Article Online
DOI: 10.1039/D5EN00784D

and more hydrophobic chains. It was previously demonstrated that pristine PS NPs are stable and resist aggregation when dispersed in pure water[117]. As water constitutes a poor solvent for hydrophobic PS, the outer layer of unmodified PS NPs is expected to contain collapsed polymer chains forming small globules[118–121]. Furthermore, conditions under which the PS NPs are produced can also affect the morphology of NP surface as well. The synthetic PS NPs are typically smooth solid spheres[52,122]. However, in real-life scenarios, the formation of PS NPs occurs via the degradation of plastics in the environment, complicated by natural aging and wear (e.g., rubbing materials against the sand, the interaction with the oxygen or metabolites of the bacterial colonies living on the surface of the material, or the exposure to UV light). Such metamorphosis can increase the physical roughness and surface-to-volume ratios in environmental nanoplastic particulates, ultimately resulting in surface chemistry modifications. Consequently, alterations in the protein corona compositions formed in these NPs and associated variations in nanotoxicity should be expected[123–126]. For example, in the case of polyethylene (PE) microplastics with sizes 1–10, 50, and 100 μm, the higher curvature of the surface was linked to elevated cytotoxicity, pro-inflammatory cytokine release, and hemolysis[127], particularly at high concentrations of PE particulate. However, it was also shown that the roughness of polymeric PS NPs can result in slower uptake[128]. However, this factor can be overridden by the presence of charges on the NP, as higher uptake rates were observed in HeLa cells for positive and rarely for negative surfactant-stabilized PS NPs, regardless of surface curvature and total surface area[128,129].

Taking into account all these factors, we model a PS NP as a single smooth uniform-density sphere of the corresponding radius, decorated with smaller neutral PS and charged beads placed around the smooth sphere mimicking a low-roughness surface with chemical modifications. For comparison purposes, we used similar parameters of the previously proposed MD model of PS NPs for protein adsorption[107]. The total number (198) of charged surface beads was placed in the outer layer to model charged PS NPs. The ζ-potentials shown in Table 1 were evaluated via Grahame equation[130] from the corresponding surface charge densities σ at the slipping plane where surface potential $\Psi_0 \approx \zeta$:

$$\sigma = \frac{\varepsilon_r \varepsilon_0 \Psi_0}{\lambda_D}$$
$$\zeta = \frac{\sigma \lambda_D}{\varepsilon_r \varepsilon_0}, \quad (9)$$

where λ_D is the Debye length, ε_r and ε_0 are the dielectric permittivities of water and vacuum, respectively. The absolute values were close to $|\zeta| \approx 2\frac{k_B T}{e} \approx 50$ mV, suggesting that the surface charge density $\sigma = 0.63e/\text{nm}^2$ corresponds to moderate to strongly charged surfaces[131]. Furthermore, considering that the carboxylic group has pK_a of about 2-5, it is expected that at pH 7.4 it should be fully ionized. In this case, the PMFs for COO^- fragment (see Figure S1c in Supporting Information) were assigned to the decorating beads. At the same time, NH_2 group is basic ($pK_a \approx 10.0$) and thus it is also expected to be fully ionized at a neutral pH. The PMFs for NH_3^+ groups shown in Figure S1d in Supporting Information were assigned to decorating beads in PS-NH_2 NP models.

Table 1 Physicochemical parameters of PS NPs used in the *UA* simulations.

NP	R_{NP}, nm	ζ, mV	Q_{tot}, e^a	$\sigma, e/\text{nm}^{2b}$
PS	5.0	0.0	0.0	0.00
PS-COOH	5.0	−47.7	−198.0	0.63
PS-NH_2	5.0	+47.7	+198.0	0.63

[a] Q_{tot} is a total charge of NP taken from Ref.[107];
[b] Charge density is calculated from $\sigma = \frac{Q_{tot}}{4\pi R_{\text{NP}}^2}$.

The radii of the beads in the outer raspberry shell were set to 0.36 nm, as estimated from the radius of gyration (r_g) of the chosen PS oligomer fragments used for parameterization of PS-AA side chain (SCA) PMFs (see Section 2.4.3). The resulting CG models of PS NPs are shown in Figure S1 in the Supplementary Materials. *UA* simulations require a set of parameters describing NP-SCA interaction (the short-range NP-SCA potentials, Hamaker constant, and specific volume values) that are assigned for each CG bead composing the NP, including decorating beads[132]. The procedure for obtaining short-range potentials for SCA-PS, SCA-COOH, and SCA-NH_2 interactions is described in the following section. The Hamaker constants and specific volume values required for pairwise interactions were evaluated using the protocol described in detail in Ref[94]. To improve the sampling of protein adsorption energies for varying roughnesses of the PS surface, 10 random rotational configurations of NP coordinates were used to obtain average adsorption affinities by *MultiSurfaceAverage.py* tool in *UA* package as previously described in work[93].

2.4.2 Obtaining Cartesian coordinates for proteins.

The coordinates of five proteins studied were taken from the Protein Data Bank: human serum albumin HSA, (1AO6[133]), human fibrinogen, FG (3GHG[134]), human IgG immunoglobulin, IGH (1HZH[135]), human complement component 3, C3 (2A73[136]), and human apolipoprotein A1, APO-AI (3K2S[137]). The choice of PDB entries was mandated by the PDB structures listed in work[107] that we use for validation. The PDB structures were preprocessed with the CHARMM-GUI PDB Reader tool[138]. The protonation state of all proteins at pH 7.4 was refined with PropKa software[139]. Any post-translational modifications (e.g., glycosylation) or co-crystallized entries were excluded. The characteristics of the selected proteins are listed in Table 2.

2.4.3 Obtaining CG PMFs for pristine and modified polymeric NPs.

The protocol for obtaining *UA* PMF profiles $w(r)$ within the 1.2-nm cut-off around the AA side chain bead from radial distribution function (RDF) $g(r)$[146] was reported previously and was followed in the current work:

View Article Online
DOI: 10.1039/D5EN00784D

Table 2 Physicochemical characteristics of proteins used in this study

Proteins	Name	PDB ID	UniProt ID	M_W, kDa[a]	Q_P, e[b]	C_P, g/L[c]	PDB resolution,Å	Chains[d]
HSA	Human Serum Albumin	1AO6	P02768	131	−15.0	35 − 50 [140]	2.50	A
C3	Complement component C3	2A73	P01024	183	−24.0	1.2 [141]	3.30	A,B
FG	Fibrinogen	3GHG	P02671	228	−14.0	2 − 4 [142]	2.90	A,D,G,J,B,E,H,K
APO-AI	Apo-Lipoprotein	3K2S	P02647	56	−8.0	1.58 [143,144]	N/A	A,B
IGH	Immunoglobulin	1HZH	P01857	150	+22.0	5.6 − 18 [145]	2.70	A,B,C,D

[a] molecular weight, calculated from PDB structure;
[b] total charge, calculated at pH 7.4;
[c] protein concentration in blood plasma.
[d] chains included in PDB of biological assembly.

$$w(r) = -k_B T \ln[g(r)] \quad (10)$$

This approach worked reasonably well for *UA* CG models of PEG core-shell NPs [93]. The RDF functions for the inversion were calculated along the distance between the centers of mass for SCA and PS or decorating beads. However, the extension of this protocol to larger fragments of CG PS may be questionable due to many-body effects. To omit the latter, the 1:1 ratio of interacting beads was considered in this study. To model the PS-SCA interaction, a single CG bead of PS chain was represented by $(C_8H_8)_{n=4}$ fragment. The simulation systems were composed of one biomolecular fragment and one PS fragment solvated by TIP3P water and neutralized by 0.15 M KCl. The temperature was set at 298.15 K in the NPT and NVT ensembles, and the pressure was at 1 bar in the NPT ensemble. The Nose–Hoover thermostat was invoked for NVT simulations, while Berendsen's weak coupling thermostat and barostat were applied for NPT runs. The system was modeled using periodic boundary conditions with an approximate primary cell size of 8.0 nm × 8.0 nm × 8.0 nm. These boxes were pre-equilibrated to obtain a proper density/pressure and were subject to 200 ns production runs to collect RDFs. All-atom molecular dynamics simulations in this study were performed with the GROMACS package [147] and the CHARMM36m [148] force field parameters with a cutoff distance 1.2 nm. RDFs for each set of SCA-material pair were calculated by the *gmx rdf* tool in GROMACS, ensuring that the distance between the two centers of mass (COM) was selected. To reduce the noise in RDF curves, a 1D Gaussian filter with a standard deviation for the Gaussian kernel equal to 2-4 is applied (*scipy.ndimage.gaussian_filter1d* Python library). RDFs were inverted as per Equation (10) to obtain CG PMFs (in k_BT). The CG potentials used in *UA* model are referenced with respect to the surface-surface separation distances, which are obtained from the potentials constructed along the distance between the planar surface of the material and the COM of SCA. To harmonize the potentials obtained from the inverted RDFs, we shifted them by the distances corresponding to the radius of gyration of the material fragment, replicating a single CG bead. The radii of gyration were obtained with the *gmx gyrate* GROMACS tool for analysis of MD trajectories. Short-range *UA* potentials for the decorating beads were obtained in a similar way. To cover various pH regimes in the *UA* CG models, ionised and nonionised analogues of COOH and NH_2 CG beads were parameterised. Final PMF sets used in *UA* simulations are shown in Figure S1.

3 Results

3.1 Individual protein adsorption onto pristine and functionalized PS NPs.

3.1.1 Preferred orientations of adsorbed proteins.

UA model can predict the lowest-energy configurations of the adsorbed proteins from adsorption heatmaps. However, it is important to note that the definition of protein adsorption energy for a single orientation located on the heatmap contains inherent uncertainty [149]. Therefore, it is advisable to approach the interpretation of a single docking configuration with some caution. Ideally, multiple minima should be evaluated, and their corresponding orientations should be cross-checked with experimental data on protein-nanomaterial complexes if such information is available. As we lack specific experimental data on the spatial configuration of protein-NP complexes to assess how well the *UA* model predicts the adsorption of individual proteins on PS NPs we will use the high-resolution atomistic MD study mentioned in [107], along with several other indirect experimental observations, served as reference points to validate our multiscale calculations. In general, the orientations of proteins adsorbed on PS-NH_2 NPs predicted by the *UA* model were visibly similar to those found in the MD study [107]. The differences noted are discussed below. The reasons for these discrepancies are also discussed in Section 3.2. The AESs and protein adsorption complexes corresponding to the lowest energy poses at AES are shown in Figures 1, 2 in the main text, and Figures S2-S5 from Supporting Information. Information on additional docking poses located on the AES are collected in Tables S1-S3 in Supporting Information (coordinates, energy rankings, and closest contacts). The locations of the lowest minima on the AES landscape for pristine PS were similar to those for negatively charged PS-COOH or positively charged PS-NH_2 NP. Analysis of the lowest-energy conformations for adsorbed proteins has revealed that diverse AA patches can be observed near the NP surfaces (see Tables S1-S3 in Supporting Information). Positively charged AAs (e.g., Lys and Arg) and aliphatic AAs were prevalent to maintain contact with pristine PS and PS-COOH NPs. For positively charged PS-NH_2 NP, the adsorption occurred through aliphatic and negatively charged side chains (e.g., Glu and Asp). Such multi-modal binding preferences occurring at the level of individual AAs facilitate protein adsorption on PS surfaces, regardless of the total protein charge, and result in multiple preferred AES docking poses characterised by a similar exothermic adsorption effect.

View Article Online
DOI: 10.1039/D5EN00784D

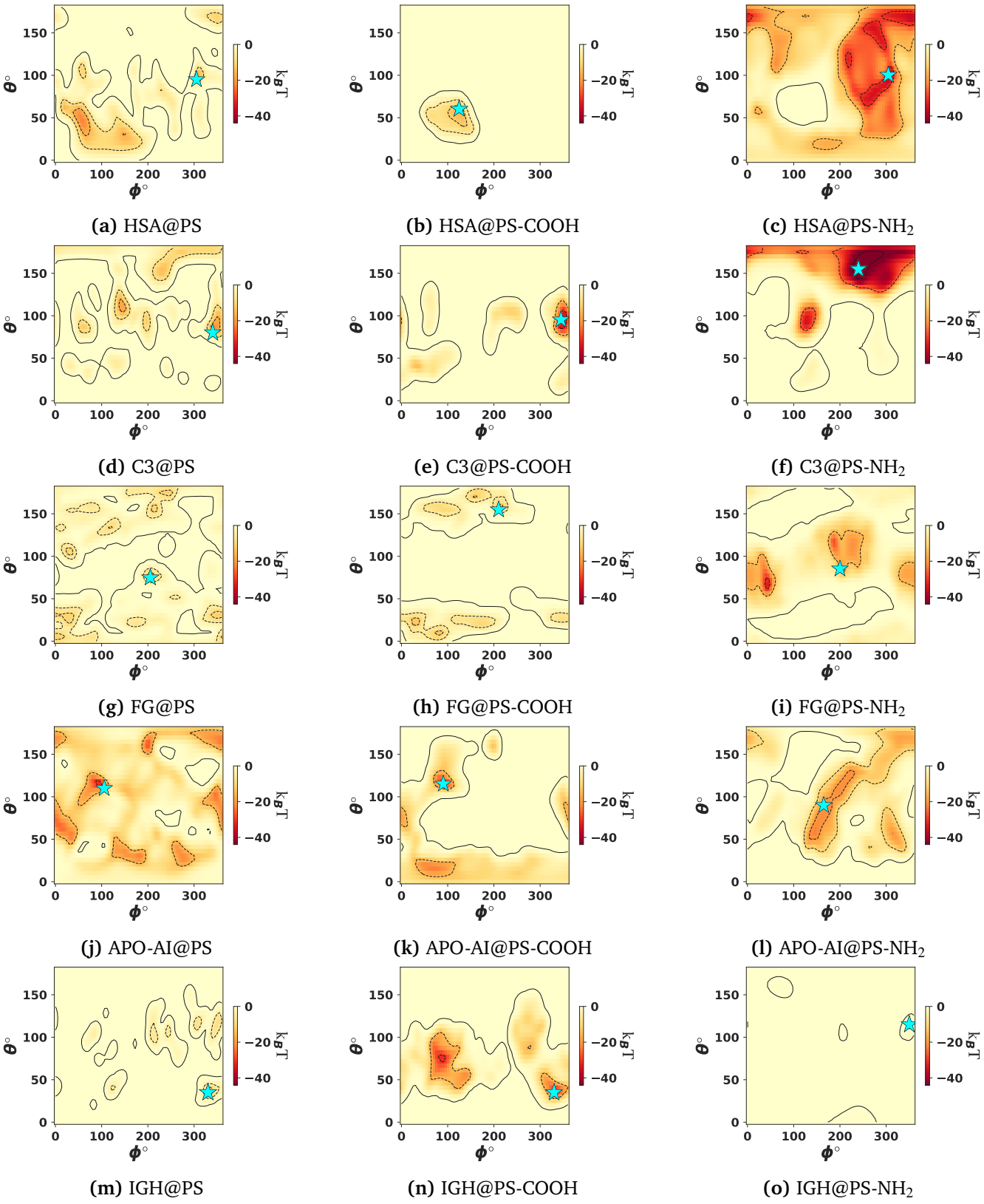

(a) HSA@PS (b) HSA@PS-COOH (c) HSA@PS-NH_2

(d) C3@PS (e) C3@PS-COOH (f) C3@PS-NH_2

(g) FG@PS (h) FG@PS-COOH (i) FG@PS-NH_2

(j) APO-AI@PS (k) APO-AI@PS-COOH (l) APO-AI@PS-NH_2

(m) IGH@PS (n) IGH@PS-COOH (o) IGH@PS-NH_2

Fig. 1 Adsorption energy surfaces (heatmaps) for one configuration of selected functionalised NPs and five proteins: serum albumin (HSA), fibrinogen (FG), immunoglobulin (IGH), complement component 3 (C3), and apolipoprotein A1 (APO-AI). This set of multiple heatmaps was used to obtain Boltzmann-average energy values shown in Figure 3. The positions of the minima are marked with the "star" signs. Contour maps were generated using identical energy ranges to emphasize the comparative intensity of interactions between specific proteins and nanoparticles. The AESs have some common features, however, it depends on the functionalization and the charge of the NPs.

View Article Online
DOI: 10.1039/D5EN00784D

3.1.1.1 Adsorption of HSA. A multi-modal mechanism of HSA adsorption on 99-nm pristine, carboxylate- and amine-modified PS NPs was noted in Ref.[150]. The authors suggested that although HSA has an overall negative charge, its surface contains a mix of positively and negatively charged AAs, creating localised binding patches accessible for oppositely charged particles. They suggested that in solution with 150 mM monovalent ions, the Debye length (κ^{-1}) is about 0.8 nm, thus, proteins and NPs should be in proximity of each other to experience strong electrostatic forces. However, at these distances, Van der Waals attraction is expected to become the primary driving mechanism for HSA adsorption, facilitated by the heterogeneous charge distribution on the protein's surface. In the present study, the HSA's AAs nearest to the NP surface were Glu16, Glu17, Hsd128, Glu131, Lys162, Thr166, and Gln170 for PS NP (Figures 2a, 2d) and Glu17, Lys162, Gln170, and Pro282 for PS-NH_2 (Figures 2c, 2f), while for PS-COOH the closest side chains were located at the loops of the $\alpha-$helixes near Glu501, Lys538, Gln580, Ala581 (Figures 2b, 2e). The NP-binding site near the residues 540-580 of the homologous BSA protein was previously reported by MD simulations of BSA interacting with pristine and modified PS NPs[151]. In HSA this binding configuration corresponds to the lowest energy docking pose for negatively charged PS-COOH NP at ($\phi = 125°; \theta = 55°$) coordinate and (see Figures 1a). The authors of MD study also noted an overlap of NP-binding sites in BSA for aminated and pristine PS plastic models vs. the carboxylated surface model of PS. Previously, it was also shown that BSA would adopt a side-on orientation while binding to pristine PS NPs with radii 30, 100, 110 nm[114]. A side-on orientation was also predicted by *UA* simulations for HSA binding onto all three models of modified PS NPs used in the current work (Figures 1a-c). Experimental studies[152] have shown that the fluorescence quenching of HSA-PS complexes, reflecting the interaction strength between the fluorophore and the quencher, decreases in the row PS-NH_2>PS-COOH>PS. In Förster Resonance Energy Transfer (FRET), the efficiency of energy transfer (E) is highly dependent on the distance (r) between the donor and acceptor molecules[153]. The efficiency is inversely proportional to the sixth power of the distance ($1/r^6$) between NP and tryptophan (Trp) and tyrosine (Tyr) residues in the protein. For HSA the closest to the PS surfaces was Tyr138 (6.7 nm for pristine and 6.8 nm for PS-NH_2 NP) and Tyr497 (5.8 nm for PS-COOH). Furthermore, the reported stronger quenching effect for amine-functionalized PS was assigned to enhanced local hydrophobicity near Tyr138 and Tyr150 AAs that can be induced by additional rearrangement of the interacting nearby protein's region. These aromatic AAs were calculated to be close to the binding site near Lys162 for HSA@PS-NH_2 *UA* docking pose with ($\phi = 305°; \theta = 95°$) rotational coordinates as shown at Figure 2i (Tyr138 and Tyr150 are highlighted in cadmium yellow colors). At least two well-defined HSA drug binding sites have been described in the literature[154]. Sudlow drug sites I and II are located near Trp214 and Arg410 AAs (highlighted at Fig. 2b in forest green and red colors, respectively). It is predicted that these residues do not directly interact with the NP surface in either PS modification, suggesting that their interaction with the NP may be irrelevant for preserving these sites. However, in the case of PS-COOH NP, disruption of this pocket may occur due to protein adsorption onto the NP via adjacent Glu501 and Lys538, potentially affecting drug-HSA interactions. This hypothesis, however, necessitates further investigation, including unfolding processes as part of nano-bio interfacial processes, although such simulations exceed the capabilities of the *UA* framework.

3.1.1.2 Adsorption of C3. The human C3 protein comprises several critical functional structural elements, including the β (residues 1-645) and α (residues 650-1641) chains[155,156]. C3 convertases cleave C3 at Ser726–Arg727, initiating the conversion of the anaphylatoxin domain or ANA (residues 650–726) into anaphylatoxin C3a and activating the C3b fragment with the thioester-containing domain (TED, residues 963–1268). The covalent attachment of C3b to antigen surfaces via a thioester bond in TED activates the complement component C3 defense mechanism against pathogens. The thioester bond (Cys988-Gln991) is shielded from reactions with small amino or hydroxyl nucleophiles (e.g., water, ammonia, methyl amines) by a hydrophobic/aromatic pocket composed of Met1378, Tyr1425, Tyr1460, and Phe1047 in native C3, becoming exposed only after proteolytic cleavage. Upon activation, C3b binds to the sugar-rich cell surfaces of viruses and pathogens, although this opsonization does not discriminate against host surface receptors. The surface-bound C3b subsequently induces phagocytosis. Residues 1496–1641 constitute a carboxy-terminal C345C or NRT domain with a netrin-like fold. The NRT domain is a target for complement inhibitors under development as therapeutics for various diseases. Inhibitor binding to this domain can prevent the formation or stability of the convertase enzymes. The domain undergoes significant structural changes during complement activation and binding events[157,158]. The C345C domain mediates key complement interactions, and dysregulation of C3 activation involving this region has been implicated in Alzheimer's disease–related neuroinflammation and synaptic loss[159]. Complement activation by polymer-coated surfaces was previously reported[160]. The activation can occur as a result of C3 direct binding to the surface (alternative pathway). For C3 protein bound to PS NPs, three favourable docking poses were observed (see Figure S4 in Supporting Information). For pristine PS the protein was bound via Leu292, Lys283 and $\alpha-$helix between Lys700 and Glu711 on ANA fragment. Similar orientation with $\alpha-$helix between Lys700 and Arg718 on ANA fragment was predicted for PS-COOH NP. And in case of PS-NH_2 NP the interaction occurred via the $\alpha-$helix between Gln1616 and Phe1637 at NRT domain. Predicted poses resonate with experimentally observed behaviour of C3 protein. For example, it was shown that binding of the NRT domain to PS-NH_2 NP could work as a nanobody inhibiting amplification of complement system activation at the C3 level[161]. Furthermore, for C3 to effectively target pathogens or damaged cells, its ANA domain must be appropriately exposed. Thus, if ANA binds to PS and PS-COOH NPs as predicted by our simulations, this interaction can potentially disrupt ANA's movement and prevent complement activation in response to pathogens. None of the PS NPs targeted the compstatin binding site near Ile389-

View Article Online
DOI: 10.1039/D5EN00784D

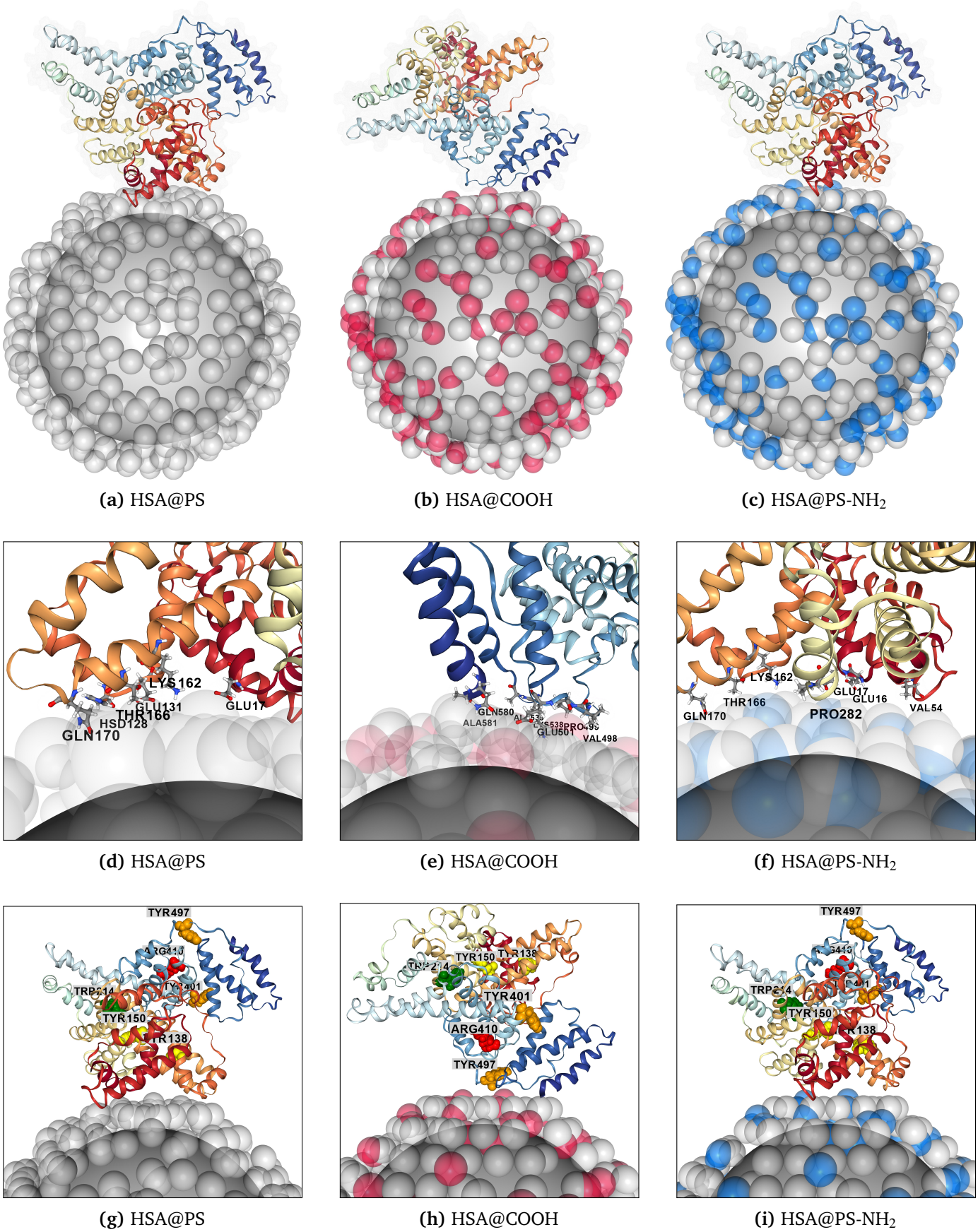

(a) HSA@PS **(b)** HSA@COOH **(c)** HSA@PS-NH_2

(d) HSA@PS **(e)** HSA@COOH **(f)** HSA@PS-NH_2

(g) HSA@PS **(h)** HSA@COOH **(i)** HSA@PS-NH_2

Fig. 2 The lowest energy configurations of HSA protein bound to various PS NPs as predicted by the *UA* modeling. Here, the coordinates of the minima (marked with the "star" symbol) were taken from adsorption heatmaps shown in Figure 1. AAs closest to the nanosurface (within 5 Å cut-off) are labeled (*d-f*). Aromatic residues relevant for fluorescence quenching of HSA-PS complexes discussed in text, Tyr138/Tyr150 and Tyr401/Tyr497, are highlighted in cadmium yellow and ochre orange colors (g-i). The Sudlow drug sites I and II near Trp214 and Arg410 AAs are also shown in forest green and red colors, respectively. The residue identifiers are the same as in the original protein PDB files.

View Article Online
DOI: 10.1039/D5EN00784D

Ser394, Arg456-Met457, and Gly489-Asp491 pocket located on β-chain[162–164] and thus shall not alter its ability to inhibit C3 activation.

3.1.1.3 Adsorption of IGH. Activation of complement can also proceed via a classical activation pathway: initial binding of immunoglobulins to biomaterials, followed by binding of complement component C1 to FC fragment of immunoglobulins[160,165,166]. Thus, complement activation of classic pathway in response to contact with artificial materials suggest the possibility of Fab-on surface orientation of immunoglobulins. It was also shown that pre-adsorption of antibodies before blood plasma/serum incubation enhances uptake of functionalized PS NP of 230 nm and 150 nm by target cells of moDCs with the CD3 receptor[167]. This uptake enhancement suggests the optimal orientation of immunoglobulin bound to PS NPs to target the CD3 receptor. Superior targeting efficacy results from substantial exposure to functional receptor binding sites on Fab1 and Fab2 in outer space (Fc-on surface bound orientation). In simulations of all-atoms[168], the three possible orientations for the adsorption of IGH onto a flat PS surface were predicted: Fab-Fab-on, Fc-on, and Fab-Fc-on orientations. In our calculations, we observed only Fab-on or Fc-on orientations. The simultaneous interaction between two subunits and the PS surface was not predicted due to a mismatch in protein and NP size, resulting in insufficient surface area available to accommodate both subunits. Our calculations indicate that the preferred orientation of IGH on pristine and functionalized PS NPs differs (see Figure S5 and Tables S1, S2, S3 in Supporting Materials). However, a very shallow minima ($E_{ads}(\phi,\theta)=-2.6k_BT$) was predicted in the case of PS-NH_2 NP where the IGH was oriented with both Fab fragments facing outward and Ile266, Gln330-Lys336 residues on the Fc facing the NP surface ($\phi=345°;\theta=110°$). While this orientation was also anticipated for pristine PS NPs ($E_{ads}(\phi,\theta)=-13.7k_BT$), a stronger adsorption minimum ($E_{ads}(\phi,\theta)=-24.6k_BT$) was expected for a different orientation ($\phi=330°;\theta=35°$). In this orientation Arg18, Arg24, Arg29, Ser67, and Asp70 in the Fab1 fragment were the closest to the surface. Similar orientation was predicted for PS-COOH NP.

3.1.1.4 Adsorption of FG. The adsorption of FG at the solid-liquid interfaces has been widely studied because of its crucial role in blood coagulation. According to SFG spectroscopy, FG forms a complete layer on pristine PS surfaces, with absorption reaching equilibrium at approximately 20,000 seconds[169,170]. Upon adsorption, FG adopts a bent conformation, where one E-D fragment lies flat and the other E-D segment stretches outward. This bending, which deviates by 30° from its linear form, occurs near the center of the FG molecule. Once bound to PS, the orientation and shape of fibrinogen do not change over time. The change of SFG intensity of N-H stretching signals (3270 cm^{-1}) from FG was also observed as a result of adsorption onto PS. At the same time, for a blank polyester surface, FG was predicted to bind to the PET surface through the D-terminus[171] similar to FG adsorption at the silicon oil-water interface. All-atom MD simulation studies of FG adsorption to mica and graphite surfaces have shown that the attachment to the surface occurred through the D the E regions[172]. In the work[173], the exploration of microelectrophoretic behavior and concentration depletion revealed two main mechanisms for FG adsorption. The first mechanism, which is more prevalent at lower ionic strengths, involves random orientation adsorption that allows FG to penetrate deeply into the fuzzy polymeric layer on the surface of NP. The second mechanism, referred to as a side-on adsorption, becomes more prevalent at $pH > 5.8$ and an ionic strength of 0.15 M. The results of our calculations show (see Figure S6) that for pristine and positively charged PS, the lowest energy of adsorption was predicted for orientations where FG approaches the PS surface at the coiled coil region between E and D domains and near the residues Phe74, Lys78, Lys81, Asp82, or Ser85 or Phe35, Ser37, Asp38, Glu39, Asp40 (see Tables S1, S2, S3 in Supporting Materials). This orientation can be considered as a side-on orientation predicted for experimental conditions close to our theoretical ones ($pH=7.0$, $I=0.15M$). Similar residues were predicted to mediate the attachment of E-domain to the surface of the EMT zeolite[174]. The adsorption onto negatively charged PS-COOH takes place near the Lys173, Asn175, and Pro260, Ala271, Asp272 residues within one of the D domains, and this can be described as an orientation that involves penetration into the polymer's surface layer.

3.1.1.5 Adsorption of APO-AI. According to our *UA* model simulations, fragments between Gln41-Lys45-Leu46-Leu47 were found near pristine and COOH-modified PS NP's surface (see Figure S7). In the case of amino-modified PS, multiple orientations with similar $E_{ads}(\phi,\theta)=-22\pm3k_BT$ were located on the AES (see Tables S1, S2, S3 in Supporting Materials). The alternative conformation was located at $\phi=310°;\theta=55°$ and had the Lys226-Glu234 patch near the surface. Unfortunately, no information on the orientation of APO-AI at the NP's surface was found in the literature to validate these docking poses.

3.1.2 The *UA* binding affinities $\langle E_{ads}^{Boltz}\rangle$.

The adsorption energies $\langle E_{ads}^{Boltz}\rangle$ calculated with *UA* are collected Figure 3). For pure PS the highest affinity was predicted for the APO-AI protein ($-60.5k_BT$), for positively charged PS-NH_2 the strongest binders were the C3 ($-65.4k_BT$) and HSA ($-50.8k_BT$) proteins, and for negatively charged PS-COOH the moderate binding energy was predicted for multiple proteins (APO-AI, IGH,C3). Predicted binding affinity $\langle E_{ads}\rangle$ for HSA protein and neutral PS NP was $-28.2k_BT$, which is higher than the previously reported experimental value of -9 kcal/mol ($-15.2k_BT$ at 298.15 K) for HSA adsorption on the larger 200-940 nm PS latex NP[175]. In case of homologically consisted bovine serum albumin (BSA) and 100 nm and 200 nm diameter carboxy-functionalised PS Fluospheres, the experimental free energy of adsorption for BSA was -30 and -35 kJ/mol (or -8.9 and $-10.4k_BT$) respectively[176]. Furthermore, the UA-calculated HSA binding trend was not in line with the adsorption affinities for the same PS NPs predicted by MD simulations of higher resolution umbrella sampling from a benchmark report[107]. The HSA adsorption free energy ΔG_{ads} reported there was calculated to decrease (the adsorption affinity to increase) from pristine PS ($-10.9k_BT$) to PS-NH_2 ($-25.2k_BT$) to PS-COOH NPs ($-93.4k_BT$). The *UA*-calculated HSA preference for modified PS was different, as the affinity increased in

View Article Online
DOI: 10.1039/D5EN00784D

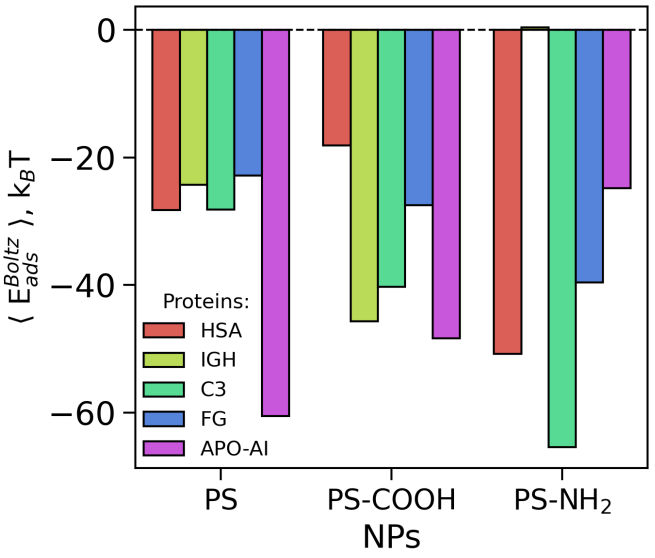

Fig. 3 Individual protein adsorption affinity ranking for 10-nm PS NPs. The Boltzmann-averaged energy values $\langle E_{ads}^{Boltz} \rangle$ were obtained by averaging over multiple adsorption energy surfaces corresponding to a set of 10 NP configurations. HSA and C3 proteins stand out with elevated adsorption affinities toward PS-NH_2 NPs.

the row: PS-NH_2 ($-50.8k_BT$) > pristine PS ($-28.4k_BT$) > PS-COOH ($-18.1k_BT$). In a comparative analysis of calculated immunoglobulin IGH adsorption affinities with isothermal titration calorimetry (ITC) data for analogous systems[177], specifically PS, PS-COOH, and PS-NH_2 NPs with radii $R = 52, 57, 51$ nm and zeta potentials $\zeta = -10, -29, 2$ mV, respectively, the following correlations were observed: the measured heats of adsorption ΔH increased in the sequence for the NPs of PS-COOH ($-99.6k_BT$), PS-NH_2 ($-39.5k_BT$), and PS ($-14.5k_BT$). In the case of *UA*-predicted affinities $\langle E_{ads}^{Boltz} \rangle$, a stronger interaction was predicted for PS-COOH ($-45.6k_BT$) and pristine PS ($-24.3k_BT$), whereas the positively charged PS-NH_2 NP repelled IGH ($0.37k_BT$). The free energies of adsorption ΔG, which include the entropy term ΔS, also did not exhibit a strong correlation[177]. This discrepancy may be attributed to protein denaturation upon binding to the NP. More negative ΔS values for carboxyl- and amino-functionalized PS suggest that protein denaturation might be more pronounced on modified PSs. However, the unfolding process cannot be modeled within the *UA* multiscale framework, which may account for such discrepancies.

In a study[178] involving 23 nm PS, 24 nm PS-COOH, and 57 nm PS-NH_2 NPs, it was observed that APO-AI has a greater affinity for PS and PS-COOH NPs than HSA or reconstituted HDL proteins. In line with this observation, our calculations have also shown that APO-AI has a higher individual binding energy than HSA for pristine and COOH-modified PS (see Figure 3). For apolipoprotein APO-AI, the *UA*-calculated binding affinity values were were exothermic, ranging from $-60.5k_BT$ (PS) to $-48.4k_BT$ (PS-COOH) to $-24.9k_BT$ (PS-NH_2).

It was shown experimentally[179] that fluorescence quenching efficiency for interaction between FG and 80nm PS NP decreased by 45.5%, 49.2%, and 55.9% for PS-COOH, PS, and PS-NH_2 NPs, suggesting that positively charged PS NPs are more likely to combine with FG and change its structure. Thermodynamic measurements indicated that the interaction between FG and PS occurs spontaneously ($\Delta G < 0$) and is mainly driven by hydrophobic interactions ($\Delta H > 0$ and $\Delta S > 0$). According to *UA*-simulations, FG also exhibits the strongest interactions with positively charged PS-NH_2, followed by PS-COOH and then pristine PS NPs (see Figure 3).

3.2 Formation of protein corona on PS NPs.

Previous studies have indicated that incubation of 80 nm PS NPs without any functionalization with human plasma results in a protein corona that significantly enhances placental transfer[180]. This effect was more pronounced compared to the PS-corona formed with BSA and dextran, which was used as a control in the experiments. After incubation of PS particles with plasma, the most abundant proteins were albumin, immunoglobulins, and apolipoproteins. At the same time, a high mean corona intensity was also observed corresponding to fibrinogen and C3 (see Table S5 in Ref.[180]). The results of our CoronaKMC simulations of competitive adsorption of selected proteins onto smaller 10-nm PS NP echo similar results. Calculations have predicted that the NP's coverage with proteins occurs from the initial seconds (Figure 4 and that the maximum load capacity is reached within 60 s of simulation time or less. Estimated the maximum load capacity for 10-nm PS NP ranges from 9-16 proteins (see *maxLoadGeom.ipynb* at GitHub archive in Supporting Materials).

As shown in Figure S8 in the supporting materials, the first 9 HSA entities are adsorbed at $t = 0.01$ s (Figure S8a) and an APO-AI binds at $t = 0.03$ s (Figure S8j) for pristine PS. In the case of PS-NH_2 NP, 12 HSA molecules are adsorbed at $t = 0.01$ s (Figure S8c) and later the number of HSA molecules drops to 0 at $t = 14.3$ s while 1 C3 molecules bind to NP at $t = 0.03$ s and reach its maximum load (17 molecules) at $t = 60.4$ s (Figure S8f). Meanwhile, 1-2 molecules of FG absorb / desorb at the surface of PS-NH_2 NP. For PS-COOH NP, the corona composition was more diverse - only APO-AI was excluded. At first, 1 APO-AI and 5 IGH molecules bind to the surface at $t = 0.01$ s (see Figures S8k, S8n). IGH reaches its maximum load at $t = 0.02$ s by replacing APO-AI and remains unchanged throughout the trajectory. Reversible binding of single C3, FG, HSA is also observed (see Figures S8k, S8e, S8h, S8b in Supporting Materials).

The calculated total protein load number (n_{max}) on the surface of NP ranging from 8 to 17 was in line with the estimated maximum protein load number. The composition of the protein corona stabilized within a 60-100 second simulation frame before reaching an adsorption plateau. The sole exception was negatively charged PS-COOH, where the maximum load of immunoglobulin heavy chain (IGH) remained nearly constant from the initial frames of the simulations, and proteins with low maximum load numbers underwent continuous exchange.

The highest total protein coverage Ω_t of PSNPs was approximately 72-81%, and this loading capacity was achieved within the first

View Article Online
DOI: 10.1039/D5EN00784D

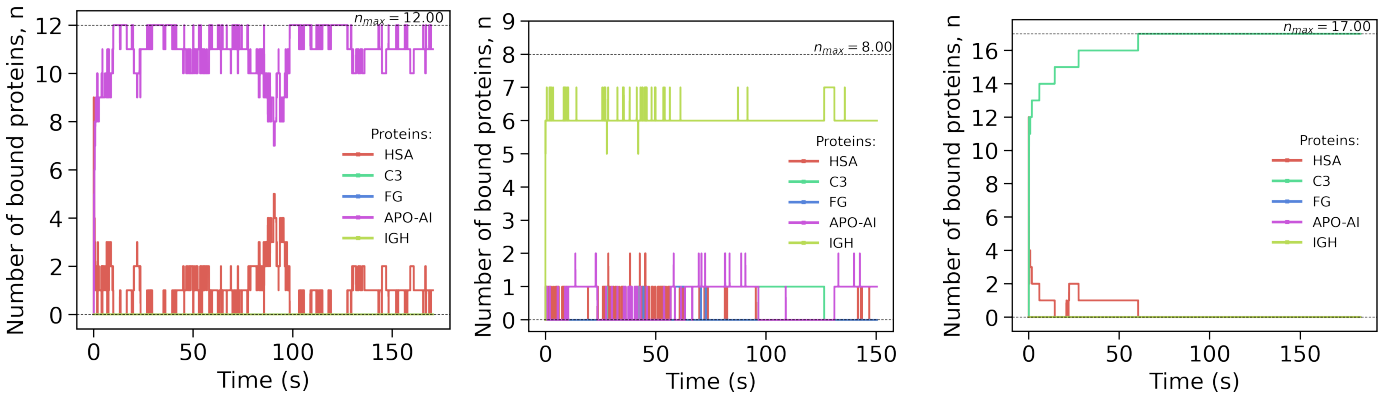

(a) PS **(b)** PS-COOH **(c)** PS-NH_2

Fig. 4 Evolution of the protein corona predicted by CoronaKMC simulations. Only non-zero coverage values for individual proteins (n_{prot}) were plotted for 180 s trajectories. The plots show that (a) adsorption on PS NPs predominantly occurring for smaller HSA albumin (max. 9 molecules at the first frames) competing with APO-AI (max. 12 molecules) protein. (b) A diverse population of corona consisting of immunoglobulins IGH (max. 7 molecules), albumins HSA (max. 2 molecules), C3 compliment protein (max. 1 molecule), and fibrinogen FG (max. 1 molecule) was predicted for PS-COOH NPs. (c) compliment component C3 (max. 17 molecules) dominated entire corona of PS-NH_2 NPs. The breakdown for each protein separately can be found in S8 in Supporting materials.

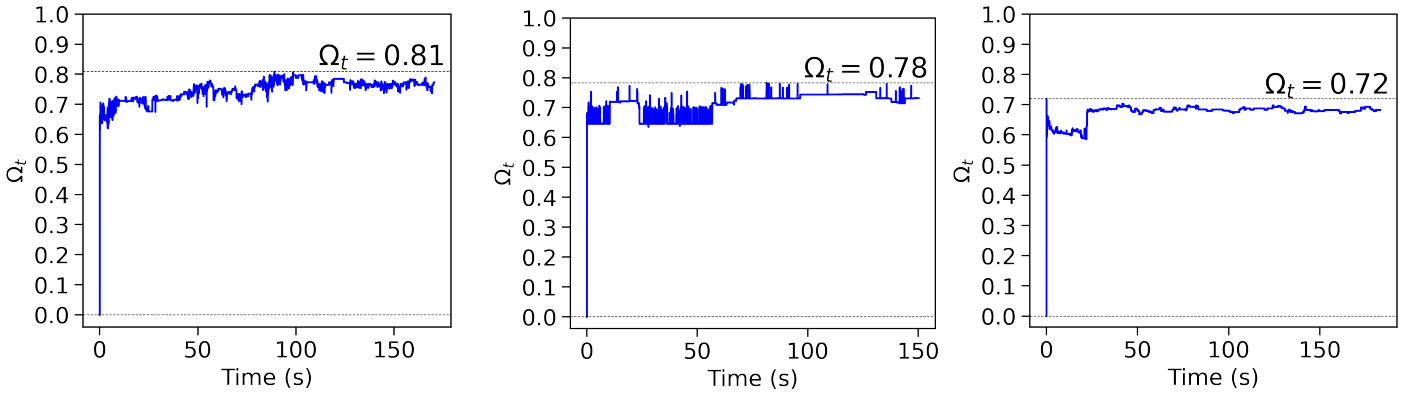

(a) PS **(b)** PS-COOH **(c)** PS-NH_2

Fig. 5 The 3 min of KMC simulation evolution of total protein load onto 10-nm PS (a), PS-COOH (b), and PS-NH_2 (c) NPs.

View Article Online
DOI: 10.1039/D5EN00784D

30 seconds of KMC simulation (see Figure 5). The results obtained echo the study[113], where the rapid formation of a protein corona comprising the most abundant plasma proteins was experimentally observed at the earliest exposure time point (0.5 min) for PS NPs charged positively (115 nm diameter) and negatively (112 nm). The authors further noted that the composition of the protein corona was established at the earliest exposure time point and did not undergo significant qualitative changes even with extended plasma exposure (480 minutes), although quantitative alterations were observed. Notably, the rankings of individual binding affinities align with the composition of the protein corona. The concentration of blood plasma proteins emerged as the second most significant factor. For example, in the case of PS-COOH, APO-AI exhibited a slightly stronger binding to the surface compared to IGH and C3. However, the immunoglobulin IGH (C_P=5.6-18 g/L) outperformed APO-AI (C_P=1.58 g/L) and C3 (C_P=1.2 g/L). Furthermore, albumin HSA (C_P=35-50 g/L), despite having the lowest binding energy, demonstrated a presence similar to that of lipoprotein APO-AI. The interplay of additional factors, such as the shape and size of the protein, in conjunction with the associated surface charge distribution that complements the shape, charge, and surface charge distribution of NPs, is anticipated to collectively determine the final "new identity" of PS NPs.

Discussions

3.3 Takeaways from CG modelling of individual protein adsorption: trends and methodology.

In our previous reports, we have examined the potential limitations of the *UA*'s predictive capabilities, which arise from the inherent constraints of the "rigid body" description of proteins and other approximations. This methodology does not account for alterations in protein conformation during the adsorption process (refer to Section "Increasing the Resolution of the *UANanoDock* Predictions" in Ref.[149] for further discussion). Moreover, within the additivity approximation, the interaction of each AA with the NP surface is optimised separately for each individual AAs, while in reality the optimal conformation may be impossible due to staric constrains within the protein globule. The model also neglects the entropic contributions associated with protein adsorption, such as protein conformational entropy loss, solvent rearrangement, and counterion release. The inconsistency in predicting binding energies, as compared to reported values, can be attributed to these simplifications. The $\langle E_{ads} \rangle$ represents an average of potential energies over sampled orientations, providing only enthalpic estimates. Consequently, *UA*-calculated adsorption affinities $\langle E_{ads} \rangle$ cannot be directly compared to experimental binding free energies. The exclusion of entropic effects typically results in weaker binding predictions; thus, the *UA* model is anticipated to overestimate the absolute strength of NP-protein interactions. Variations in experimental conditions, such as larger NPs, pH, and ionic strength of the buffers used, may further exacerbate these discrepancies. Experimental investigations into protein adsorption onto PS NPs indicate the potential for protein unfolding; however, the secondary structure elements can be either preserved or even stabilised in the presence of NPs. Consequently, the errors associated with "rigid" proteins can vary in absolute value, contingent upon the preserved stability of the secondary structure. The study by Alemie et al.[181] demonstrated that the adsorption of immunoglobulin IGH onto PS NPs with various coatings containing amino and carboxylic groups, such as allylamine, 2-methyl-2-oxazoline, or acrylic acid, resulted in denaturation. The circular dichroism (CD) spectra indicated that IGH's secondary structure exhibited a substantial presence of β-sheets and turns on NH_2-coatings, whereas some α-helices were stabilized on coatings with COOH groups. In a study[178], it was shown that when APO-AI binds to PS or PS-COOH particles, there is an increase in the α-helical signal in CD spectra, suggesting that this part of the structure is either stabilized or enhanced. In contrast, the formation of the APO-AI-PS-NH_2 complex reduces the CD signal for APO-AI, with this effect becoming more significant at higher particle concentrations. This indicates that the binding with positively charged particles may disrupt the secondary structure of APO-AI. On the other hand, protein flexibility can impact the stoichiometry of adsorption: for example it was shown that FG due to its high flexibility at the coiled-coil region[172,182] can bind to two separate NPs, potentially changing particle aggregation state[183]. Hinge bending in FG may also play an important role in fibrin polymerisation, as it can provide the necessary flexibility to accommodate new molecules in the growing fibre and thus can impact the regulation of blood clotting. Thus, it is advisable to include multiple protein conformations to evaluate protein adsorption with "rigid body" approach implemented in *UA* or introduce other treatments of protein flexibility. Regarding the potential rearrangements of polymeric NPs upon interaction with proteins, the application of the "rigid body" approximation to the NP may introduce additional errors in estimations of adsorption energies. This is due to the significant energy changes associated with such interactions, which cannot be directly captured in the multiscale *UA* model. Technically, these degrees of freedom can be accounted for through extended simulations with enhanced sampling within an all-atom MD framework. However, in practice, such simulations require enormous computing resources and can only be applied to study a limited number of proteins. A further NP-linked source of discrepancy between the results obtained from *UA* and those reported in all-atom MD simulations, as documented in the benchmarking report[107], is the relatively high sphericity of the *UA* CG raspberry models of NPs compared to the shape of MD-simulated polymeric nanoclusters. It is important to note, however, that the *UA* values account for the contributions of proteins interacting with various segments of the NP surface (10 NP orientations were included), potentially offering a more accurate representation of experimental conditions. Facilitating such comprehensive scanning of the entire NP surface in MD simulations is challenging due to the substantial system sizes involved. The *UA* adsorption affinities partially correlated to the protein charge (see Figure 6). The stronger adsorption for positively-charged PS-NH_2 NPs (as compared to pristine PS NPs) was predicted for negatively charged proteins, for example C3, HSA, and FG proteins with a total protein charge $Q_P = -24.0e$, $-15.0e$, and $-14.0e$, respectively. Similarly, the most positively

View Article Online
DOI: 10.1039/D5EN00784D

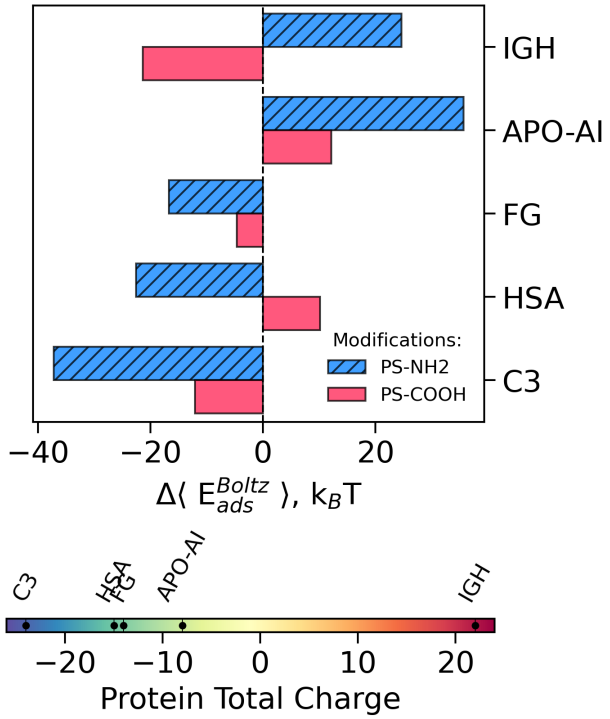

Fig. 6 The change in Boltzmann-averaged energy values $\langle E_{ads}^{Boltz} \rangle$ between neutral and charged PS NPs for proteins. The more negative the $\Delta \langle E_{ads}^{Boltz} \rangle$ value, the stronger the predicted adsorption. The more positive the $\Delta \langle E_{ads}^{Boltz} \rangle$ value, the higher protein-NP repulsion. The electrostatic attraction/repulsion plays the substantial role in protein adsorption, as shift from neutral PS NPs to positively-charged PS-NH_2 NPs results in stronger attraction of negatively charged proteins. However, for negatively-charged PS-COOH NPs this trend is not straightforward.

charged protein IGH ($Q_P = +22.0e$) had the strong preference for negatively-charged PS-COOH NPs and the least affinity for positively-charged PS-NH_2 NPs. Thus, the electrostatic attraction and repulsion are expected to play the substantial role in protein adsorption onto modified PS NPs. However this trend is not linear. For example, the adsorption of C3 protein ($Q_P = -24.0e$) was also improved when the PS NP become functionalised with negatively charged carboxylate groups. At the same time, the APO-AI protein, regardless its moderate negative charge ($Q_P = -8.0e$) has shown the least preference for positively-charged PS-NH_2 NPs as compared to pristine. These trends can indicate that protein adsorption onto PS NPs is a complex process that is regulated by various contributions and not exclusively by electrostatic forces. Furthermore, the sensitivity of the CoronaKMC model to initial parameters indicates that varying blood plasma compositions, represented by different initial protein concentrations, will result in different coronas. Moreover, as previously noted, PS nanotoxicity demonstrates size-dependent characteristics. To accurately predict NP toxicity, it is essential to consider a realistic distribution of NP sizes present in the environment, rather than assuming a uniform 10 nm NP size. Such variations in NP size may impact not only the electrostatic interactions between proteins and NPs but also potentially lead to NP agglomeration under real-world conditions. This agglomeration could alter the size of PS clusters and further change the content of the corona [184,185].

3.4 Corona of PS NPs and possible implications for environmental nanotoxicology and medicine.

The APO-AI apolipoprotein, immunoglobulin IGH, complement component C3 and serum albumin HSA were predicted as the most abundant in the protein corona of pristine and modified 10 nm PS NP in our calculations. The APO-AI apolipoprotein, immunoglobulin IGH, complement component C3 and serum albumin HSA were predicted as the most abundant in the protein corona of pristine and modified 10 nm PS NP in our calculations. These abundances can result in various outcomes. For example, The presence of IGH in the protein corona can enhance the opsonisation of NPs, facilitating the immune system's identification and removal of PS NPs, and potentially increasing the NPs' immunotoxicity by triggering an undesirable immune response [186], a complication undesirable for drug nanocarriers. A minimal number of surface-bound immunoglobulin molecules was sufficient to trigger complement activation in response to superparamagnetic iron oxide (SPIO) nanoworms [187], indicating that natural antibodies play a crucial role in C3 opsonization. Analogous immune complement activation was observed for PS-coated QCM-D sensor surfaces [188]. Experimental observations of the activation of C-related pathways in pig and human serum in response to exposure to PS NPs were also reported [189]. Activation of the complement system via the C3-associated pathway is commonly associated with the immune response to pathogens and with pro-inflammatory effects [190,191]. The prolonged activation of this mechanism can lead to inflammation and tissue damage [192]. The same pathway was also linked to neurological disorders [193,194]. Interaction with the C3 proteins was reported for various nano-

View Article Online
DOI: 10.1039/D5EN00784D

materials, and it was shown that C3 protein bound directly to the foreign surface can be replaced[195]. In our KMC simulations, the C3 adsorption was dominated in the case of negatively charged PS-NH_2 NPs and less dominant for negatively charged PS-COOH NPs. As a consequence of C-activation triggered by interaction between complement component C3 and the NP, the use of PS NPs as intravenous material for biomedical NP-based applications requires caution due to potential immunological risks. Yet, these NPs might be useful, as it was shown that the C3-activation process can be harnessed to regulate tumour growth[196]. Apolipoproteins, as well as lipoprotein particles, were found to be the main adsorbates on polymeric biomaterial surfaces[197–199]. The adsorption of the APO-AI protein from the bloodstream onto silica NPs (SiNPs) has demonstrated an initial reduction in the cytotoxic and pro-inflammatory effects of SiNPs. The subsequent rapid clearance of NPs coated with the protein corona resulted in a depletion of APO-AI, leading to cardiovascular damage and atherosclerosis[200]. Moreover, the interaction of APO-AI with NPs can be influenced by the mode of exposure. The respiratory exposure of mice to SiNPs led to the preadsorption of pulmonary surfactants, which ultimately resulted in stronger adsorption of APO-AI from the bloodstream. Due to the presence of APO-AI in the corona of pristine hydrophobic PS NPs (Figure 4a), effects similar to SiNPs may be expected to occur from exposure to engineered or freshly synthesized PS NPs. The expected primary adsorption of HSA can be viewed as beneficial factor if PS NPs are intended to act as a drug carriers, as HSA adsorption is known to promote NP uptake[201]. Moreover, albumin plays a role in transporting both exogenous and endogenous ligands in the bloodstream, such as fatty acids, hormones, and AAs, which typically bind to its two sites[202], effectively functioning as a "nano-drug" itself. The combination of HSA with NP can be used to develop a versatile drug delivery system, offering advantages such as reduced toxicity, improved drug distribution, and the potential to overcome multidrug resistance[203,204]. Nevertheless, there are drawbacks to employing PS NPs as drug nanocarriers, as albumin's interaction with NP can negatively impact the pharmacodynamics and pharmacokinetics of drugs[205,206]. For example, the presence of NP led to a reduction in the stoichiometry coefficient of HSA-paracetamol from 2 to 0.3 due to the loss of paracetamol binding sites in HSA[207]. Docking studies[208] have identified two binding sites in HSA for paracetamol—Sudlow sites I and II (see Figure 2). Although there might not be a direct interaction with the sites, the NP binding in proximity to the paracetamol site could cause structural changes in Sudlow's sites, thereby affecting the efficiency of paracetamol binding. The presence of FG in the corona was predicted only for PS-COOH NP (see Figures 4b). As a result of this interaction, the NP can weakly deplete FG from the blood. This can modulate thrombosis and inflammation without compromising hemostasis, demonstrating the potential to treat fibrinogen-driven pathologies[209]. At the same time, triggering of inflammatory cascades can be expected. It was demonstrated for negatively charged poly(acrylic acid)-conjugated gold NP, that protein unfolding can improve FG interactions with the Mac-1 integrin receptor[183,210]. In conclusion, the processes previously discussed may have detrimental effects on human health as a result of long-term exposure to polymeric waste in the environment. As the accumulation of polymeric materials in natural settings increases, so does the bioaccumulation of these substances, potentially leading to the processes mentioned earlier. The extensive distribution of micro and nanoplastic particles, along with other pollutants[152,211], raises the probability of cell uptake of PS NPs with co-adsorbed environmental contaminants, which can intensify the nanotoxicity of PS particles. Moreover, studies have indicated that the adsorption of plasma blood proteins onto PS NPs slows their aggregation and significantly enhances their colloidal stability[212–216]. This situation could pose a potential threat to human health as it may result in prolonged environmental exposure, necessitating further research.

Conclusions

The key novelty of reported work is an application of a multiscale *UA* technique to predict interactions between PS nanoplastics, a prevalent industrial and environmental polymeric pollutant, and the five most abundant human blood plasma proteins (albumin, fibrinogen, immunoglobulin, apolipoprotein, and complement component C3 proteins). As a part of our ongoing efforts in developing *UA*, we have introduced a new set of coarse-grained parameters of PS-AA interactions, required to evaluate the binding affinity for other proteins with functionalized PS NPs. Using novel parameters, we predicted the protein coronas of charged and neutral PS NPs through a competitive adsorption model (*UA/NPCoronaPredict*) incorporating the most abundant human blood plasma proteins. Our analysis has shown that apolipoprotein APO-AI, immunoglobulin IGH, and complement component C3 are the predominant proteins in the coronas of pristine, negatively, and positively charged PS NPs, respectively. Consequently, PS NPs are anticipated to elicit an immune response. Consistent with previous predictions, our findings suggest that charged PS NPs are likely to exhibit stronger interactions with plasma proteins. Therefore, natural surface wear processes can chemically and physically alter the outer layer of NPs, potentially leading to an increase in the nanotoxicity of PS NPs following their inhalation or ingestion. The presented parameterisation extends the capacity of the *UA/CoronaKMC* method for modelling micro- and nanoplastics and provides data for machine learning and "safe and sustainable by design" pre-assessment of novel polymers.

Author contributions

Conceptualization, J.S.; methodology, J.S.; testing, O.M.; supervision, V.L., J.S.; writing – original draft preparation, J.S.; writing – review and editing, J.S., V.L.; funding acquisition, V.L.

Conflicts of interest

There are no conflicts to declare.

Data availability

Additional data is available from Supporting Information online: LINK. The PDF file contains a visualisation of the PS NPs multiscale models used in the work, a visualization of the lowest energy complexes corresponding to minima found at the adsorption heatmaps; tables for multiple adsorption poses

View Article Online
DOI: 10.1039/D5EN00784D

of protein-NP complexes and corresponding AAs, nearest to the NP's surface. The PDB structures of predicted complexes (lowest energies) and the Jupiter Notebook for their visualization, PS potentials, and *UA* configurational files are available via GitHub link: https://github.com/juliasubbotina/uaCoronaPS. The latest official release of *UA/NPCoronaPredict* package (including material parameters, examples of required files, and post-processing tools) can be found here: https://github.com/ucd-softmatterlab/NPCoronaPredict.

Acknowledgements

The authors acknowledge the Irish Centre for High-End Computing (ICHEC) and the ResearchIT Sonic cluster, which was funded by UCD IT Services and the Research Office, for the provision of computational facilities and support. This work was funded by Science Foundation of Ireland grant, 16/IA/4506 "Quantitative Modeling of Bionano Interface", EU Horizon 2020 grant NanoSolveIT, grant agreement 814572, EU Horizon Europe grant nanoPASS, grant agreement 101092741, and EU Marie Sklodowska-Curie Action CompSafeNano (grant agreement 101008099).

References

1 B. J. Seewoo, E. V. Wong, Y. R. Mulders, L. M. Goodes, E. Eroglu, M. Brunner, A. Gozt, P. Toshniwal, C. Symeonides and S. A. Dunlop, *Heliyon*, 2024, **10**, e32912.

2 OECD, *Global Plastics Outlook*, 2022, p. 201.

3 H. S. Charlton-Howard, A. L. Bond, J. Rivers-Auty and J. L. Lavers, *Journal of Hazardous Materials*, 2023, **450**, 131090.

4 L. Lebreton, B. Slat, F. Ferrari, B. Sainte-Rose, J. Aitken, R. Marthouse, S. Hajbane, S. Cunsolo, A. Schwarz, A. Levivier, K. Noble, P. Debeljak, H. Maral, R. Schoeneich-Argent, R. Brambini and J. Reisser, *Scientific Reports*, 2018, **8**, 4666.

5 T. K. Dey, M. Rasel, T. Roy, M. E. Uddin, B. K. Pramanik and M. Jamal, *Science of The Total Environment*, 2023, **867**, 161390.

6 C. C. Gaylarde, J. A. Baptista Neto and E. M. da Fonseca, *Environmental Pollution*, 2021, **272**, 115950.

7 S. Lambert and M. Wagner, *Chemosphere*, 2016, **145**, 265.

8 M. Shen, Y. Zhang, Y. Zhu, B. Song, G. Zeng, D. Hu, X. Wen and X. Ren, *Environmental Pollution*, 2019, **252**, 511–521.

9 K. Mattsson, S. Jocic, I. Doverbratt and L.-A. Hansson, *Microplastic Contamination in Aquatic Environments*, 2018, pp. 379–399.

10 M. A. Bhat, K. Gedik and E. O. Gaga, *Air Quality, Atmosphere & Health 2022 16:2*, 2022, **16**, 233–262.

11 A. Wahl, C. Le Juge, M. Davranche, H. El Hadri, B. Grassl, S. Reynaud and J. Gigault, *Chemosphere*, 2021, **262**, 127784.

12 Y. Liu, H. Shao, J. Liu, R. Cao, E. Shang, S. Liu and Y. Li, *Soil use and management*, 2021, **37**, 224–242.

13 D. Materić, H. A. Kjær, P. Vallelonga, J.-L. Tison, T. Röckmann and R. Holzinger, *Environmental Research*, 2022, **208**, 112741.

14 M. Bergmann, F. Collard, J. Fabres, G. W. Gabrielsen, J. F. Provencher, C. M. Rochman, E. van Sebille and M. B. Tekman, 2022, **3**, 323–337.

15 Q. Liu, Z. Chen, Y. Chen, F. Yang, W. Yao and Y. Xie, *Journal of Agricultural and Food Chemistry*, 2021, **69**, 10450–10468.

16 H. Lai, X. Liu and M. Qu, *Nanomaterials*, 2022, **12**, 1298.

17 S. Kihara, I. Köper, J. P. Mata and D. J. McGillivray, *Advances in Colloid and Interface Science*, 2021, **288**, 102337.

18 N. Zhang, Y. B. Li, H. R. He, J. F. Zhang and G. S. Ma, *Science of The Total Environment*, 2021, **767**, 144345.

19 A. Ragusa, A. Svelato, C. Santacroce, P. Catalano, V. Notarstefano, O. Carnevali, F. Papa, M. C. A. Rongioletti, F. Baiocco, S. Draghi *et al.*, *Environment International*, 2021, **146**, 106274.

20 A. Nihart, M. Garcia, E. El Hayek *et al.*, *Nature Medicine*, 2025, **31**, 1114–1119.

21 Q. Shi, J. Tang, R. Liu and L. Wang, *Critical Reviews in Environmental Science and Technology*, 2022, **52**, 3863–3895.

22 A. Katsumiti, M. P. Losada-Carrillo, M. Barros and M. P. Cajaraville, *Scientific Reports*, 2021, **11**, 22396.

23 N. Meides, T. Menzel, B. Poetzschner, M. G. Löder, U. Mansfeld, P. Strohriegl, V. Altstaedt and J. Senker, *Environmental science & technology*, 2021, **55**, 7930–7938.

24 L. Ding, Z. Ouyang, P. Liu, T. Wang, H. Jia and X. Guo, *Science of The Total Environment*, 2022, **802**, 149840.

25 A. Delacuvellerie, S. Benali, V. Cyriaque, S. Moins, J. Raquez, S. Gobert and R. Wattiez, *Journal of hazardous materials*, 2021, **419**, 126526.

26 T. Morohoshi, T. Oi, H. Aiso, T. Suzuki, T. Okura and S. Sato, *Microbes and Environments*, 2018, **33**, 332 – 335.

27 C. Odobel, C. Dussud, L. Philip, G. Derippe, M. Lauters, B. Eyheraguibel, G. Burgaud, A. ter Halle, A. Meistertzheim, S. Bruzaud, V. Barbe and J. Ghiglione, *Frontiers in Microbiology*, 2021, **12**, year.

28 V. Viljakainen and L. Hug, *Computational and Structural Biotechnology Journal*, 2021, **19**, 6191 – 6200.

29 C. R. M, A. Debroy, M. Nirmala and A. Mukherjee, *RSC Advances*, 2023, **13**, 22905 – 22917.

30 P. A. Athulya and N. Chandrasekaran, *Journal of Molecular Liquids*, 2023.

31 H.-J. Zhang, S. Li, X.-L. Wang, K.-D. Zhang, H.-T. Fang, X. Wu, Z. Huang, W. Jiang, L. Yang, Q.-G. Tan *et al.*, *Nature Communications*, 2025.

32 S. Shan, Y. Zhang, H. W. Zhao, T. Zeng and X. Zhao, *Chemosphere*, 2022, 134261.

33 M. Ayer, M. Schuster, I. Gruber, C. Blatti, E. Kaba, G. U. Enzmann, O. Burri, R. Guiet, A. Seitz, B. Engelhardt and H. Klok, *Advanced Healthcare Materials*, 2020, **10**, year.

34 S. Shan, Y. Zhang, H. Zhao, T. Zeng and X. Zhao, *Chemosphere*, 2022, **298**, 134261.

35 M. Prüst, J. Meijer and R. H. S. Westerink, *Particle and Fibre Toxicology*, 2020, **17**, 24.

36 V. Kopatz, K. Wen, T. Kovács, A. S. Keimowitz, V. Pichler, J. Widder, A. D. Vethaak, O. Hollóczki and L. Kenner, *Nanomaterials*, 2023, **13**, 1404.

View Article Online
DOI: 10.1039/D5EN00784D

37 X. Liu, Y. Zhao, J. Dou, Q. Hou, J. Cheng and X. Jiang, *Nano Letters*, 2022, **22**, 1091–1099.

38 M. P. Monopoli, C. Åberg, A. Salvati and K. A. Dawson, *Nature Nanotechnology*, 2012, **7**, 779–786.

39 C. D. Walkey, J. B. Olsen, F. Song, R. Liu, H. Guo, D. W. H. Olsen, Y. Cohen, A. Emili and W. C. W. Chan, *ACS Nano*, 2014, **8**, 2439–2455.

40 Y. K. Lee, E.-J. Choi, T. J. Webster, S.-H. Kim and D. Khang, *International journal of nanomedicine*, 2015, **10**, 97–113.

41 D. Westmeier, R. H. Stauber and D. Docter, *Toxicology and applied pharmacology*, 2016, **299**, 53–57.

42 A. Lesniak, F. Fenaroli, M. P. Monopoli, C. Åberg, K. A. Dawson and A. Salvati, *ACS nano*, 2012, **6**, 5845–5857.

43 V. Francia, K. Yang, S. Deville, C. Reker-Smit, I. Nelissen and A. Salvati, *ACS nano*, 2019, **13**, 11107–11121.

44 N. Bertrand, P. Grenier, M. Mahmoudi, E. Lima, E. A. Appel, F. Dormont, J.-M. Lim, R. Karnik, R. Langer and O. Farokhzad, *Nature Communications*, 2017, **8**, year.

45 H. Leslie and M. Depledge, *Environment International*, 2020, **142**, 105807.

46 K. Kadac-Czapska, E. Knez, M. Gierszewska, E. Olewnik-Kruszkowska and M. Grembecka, *Materials*, 2023, **16**, year.

47 T. Kögel, Ørjan Bjorøy, B. Toto, A. M. Bienfait and M. Sanden, *Science of The Total Environment*, 2020, **709**, 136050.

48 T. Roy, T. K. Dey and M. Jamal, *Environmental Monitoring and Assessment*, 2022, **195**, 27.

49 A. Banerjee and W. L. Shelver, *Science of The Total Environment*, 2021, **755**, 142518.

50 D. M. Mitrano, P. Wick and B. Nowack, *Nature Nanotechnology*, 2021, 1–10.

51 EU Commission Report, *Nanoplastics: state of knowledge and environmental and human health impacts*, 2023.

52 L. M. A. Martin, N. Gan, E. Wang, M. Merrill and W. Xu, *Environmental pollution (Barking, Essex : 1987)*, 2022, **292**, 118442.

53 W. Bu, Y. Cui, Y. Jin, X. Wang, M. Jiang, R. Huang, J. Egbobe, X. Zhao and J. Tang, *Toxics*, 2024, **12**, year.

54 C. M. Cary, G. M. DeLoid, Z. Yang, D. Bitounis, M. Polunas, M. J. Goedken, B. Buckley, B. Cheatham, P. A. Stapleton and P. Demokritou, *Nanomaterials*, 2023, **13**, year.

55 S. B. Fournier, J. N. D'Errico, D. S. Adler, S. Kollontzi, M. J. Goedken, L. Fabris, E. J. Yurkow and P. A. Stapleton, *Particle and Fibre Toxicology*, 2020, **17**, 55.

56 B. Jeong, J. Y. Baek, J. Koo, S. Park, Y.-K. Ryu, K.-S. Kim, S. Zhang, C. Chung, R. Dogan, H.-S. Choi, D. Um, T.-K. Kim and Wang, *Journal of Hazardous Materials*, 2022, **426**, 127815.

57 L. Zeng, C. Zhou, W. Xu, Y. Huang, W. Wang, Z. Ma, J. Huang, J. Li, L. Hu, Y. Xue, T. Luo and L. Zheng, *Ecotoxicology and environmental safety*, 2023, **257**, 114941.

58 Y. Wang, K. Xu, X. Gao, Z. Wei, Q. Han, S. Wang, W. Du and M. Chen, *Particle and Fibre Toxicology*, 2024, **21**, year.

59 J. Zhao, N. V. Adiele, D. Gomes, M. V. Malovichko, D. J. Conklin, A. Ekuban, J. Luo, T. C. Gripshover, W. H. Watson, M. Banerjee, M. L. Smith, E. Rouchka, R. Xu, X. Zhang, D. D. Gondim, M. C. Cave and T. E. O'Toole, *Toxicological sciences : an official journal of the Society of Toxicology*, 2024.

60 I. F. Syarifah, R. M. Hasby, O. Taupiqurrohman and M. Mahroji, *Biological Environment and Pollution*, 2025.

61 X. Fan, X. Wei, H. Hu, B. Zhang, D. Yang, H. Du, R. Zhu, X. Sun, Y. Oh and N. Gu, *Chemosphere*, 2022, **288**, 132607.

62 B. Meesaragandla, D. O. Blessing, S. Karanth, A. Rong, N. Geist and M. Delcea, *Macromolecular bioscience*, 2023, e2200464.

63 L. Rubio, I. Barguilla, J. Domenech, R. Marcos and A. Hernández, *Journal of hazardous materials*, 2020, **398**, 122900.

64 Y. Kitagishi, M. Kobayashi, K. Kikuta and S. Matsuda, *Depression research and treatment*, 2012, **2012**, 752563.

65 C. Chu, Y. Zhang, Q. Liu, Y. Pang, Y. Niu and R. Zhang, *Ecotoxicology and environmental safety*, 2022, **241**, 113785.

66 J. Chen, L. Yan, Y. Zhang, X. Liu, Y. Wei, Y. Zhao, K. Li, Y. Shi, H. Liu, W. Lai, L. Tian and B. Lin, *Journal of Nanobiotechnology*, 2024, **22**, year.

67 L. Zou, X. Xu, Y. Wang, F. Lin, C. Zhang, R. Liu, X. Hou, J. Wang, X. Jiang, Q. Zhang and L. Li, *Environmental science technology*, 2024.

68 Y. Chen, Y. Nan, L. Xu, A. Dai, R. M. M. Orteg, M. Ma, Y. Zeng and J. Li, *Particle and Fibre Toxicology*, 2025, **22**, year.

69 S. Shan, D. Cheng, H. Li, W. Yao, R. Kou, J. Ji, N. Liu, T. Zeng and X. Zhao, *Journal of hazardous materials*, 2025, **489**, 137615.

70 X. Liang, G. Huang, Y. Wang, N. Andrikopoulos, H. Tang, F. Ding, Y. Li and P. C. Ke, *ACS nano*, 2025, **19**, 5475–5492.

71 A. Jeong, S. J. Park, E. J. Lee and K. W. Kim, *Journal of Hazardous Materials*, 2024, **465**, 133289.

72 X. Liang, N. Andrikopoulos, H. Tang, Y. Wang, F. Ding and P. C. Ke, *Small*, 2024, **20**, 2308753.

73 B. Liang, Y. Huang, Y. Zhong, Z. Li, R. Ye, B. Wang, B. Zhang, H. Meng, X. Lin, J. Du *et al.*, *Journal of hazardous materials*, 2022, **430**, 128459.

74 Z. Liu, A. Sokratian, A. M. Duda, E. Xu, C. Stanhope, A. Fu, S. Strader, H. Li, Y. Yuan, B. G. Bobay, J. Sipe, K. Bai, I. Lundgaard, N. Liu, B. Hernandez, C. B. Rickman, S. E. Miller and A. West, *Research Square*, 2023.

75 N. Tripathi, F. Saudrais, M. Rysak, L. Pieri, S. Pin, G. Roma, J.-P. Renault and Y. Boulard, *Biomacromolecules*, 2024.

76 S. J. Park, *International Journal of Nanomedicine*, 2020, **15**, 5783 – 5802.

77 N. Liu, M. Tang and J. Ding, *Chemosphere*, 2019, **245**, 125624.

78 C. Corbo, R. Molinaro, A. Parodi, N. T. T. Furman, F. Salvatore and E. Tasciotti, *Nanomedicine*, 2016, **11 1**, 81–100.

79 E. Wyrzykowska, A. Mikolajczyk, I. Lynch, N. Jeliazkova, N. Kochev, H. Sarimveis, P. Doganis, P. Karatzas, A. Afantitis, G. Melagraki, A. Serra, D. Greco, J. Subbotina, V. Lobaskin, M. A. Bañares, E. Valsami-Jones, K. Jagiello and T. Puzyn,

View Article Online
DOI: 10.1039/D5EN00784D

Nature Nanotechnology, 2022, **17**, 924–932.

80 G. Mancardi, A. Mikolajczyk, V. K. Annapoorani, A. Bahl, K. Blekos, J. Burk, Y. A. Çetin, K. Chairetakis, S. Dutta, L. Escorihuela *et al.*, *Materials Today*, 2023, **67**, 344–370.

81 V. Lobaskin, D. Power, H. Lopez and S. Poggio, *Computational Nanotoxicology*, 2019.

82 O. Vilanova, J. J. Mittag, P. M. Kelly, S. Milani, K. A. Dawson, J. O. Rädler and G. Franzese, *ACS Nano*, 2016, **10**, 10842–10850.

83 I. Hasenkopf, R. Mills-Goodlet, L. Johnson, I. Rouse, M. Geppert, A. Duschl, D. Maier, V. Lobaskin, I. Lynch and M. Himly, *Nano Today*, 2022.

84 P. Sarker, M. S. J. Sajib, X. Tao and T. Wei, *The journal of physical chemistry. B*, 2022.

85 H. Lee, *Pharmaceutics*, 2024, **16**, year.

86 O. Vilanova, A. Martinez-Serra, M. Monopoli and G. Franzese, *Frontiers in Nanotechnology*, 2024.

87 Z. Ban, P. Yuan, F. Yu, T. Peng, Q. Zhou and X. Hu, *Proceedings of the National Academy of Sciences of the United States of America*, 2020, **117**, 10492 – 10499.

88 J. Huzar, R. Coreas, M. Landry and G. Tikhomirov, *ACS Nano*, 2025, **19**, 4333 – 4345.

89 X. Fu, C. Yang, Y. Su, C. Liu, H. Qiu, Y. Yu, G. Su, Q. Zhang, L. Wei, F. Cui, Q. Zou and Z. Zhang, *Research*, 2024, **7**, year.

90 D. Power, I. Rouse, S. Poggio, E. Brandt, H. Lopez, A. Lyubartsev and V. Lobaskin, *Modelling and Simulation in Materials Science and Engineering*, 2019, **27**, 084003.

91 I. Rouse and V. Lobaskin, *Biophysical Journal*, 2021, **120**, 4457–4471.

92 J. Subbotina and V. Lobaskin, *The Journal of Physical Chemistry B*, 2022, **126**, 1301–1314.

93 J. Subbotina, I. Rouse and V. Lobaskin, *Nanoscale*, 2023, **15**, 13371–13383.

94 I. Rouse, D. Power, J. Subbotina and V. Lobaskin, *Journal of Chemical Information and Modeling*, 2024, **64**, 7525–7543.

95 P. Mosaddeghi Amini, J. Subbotina and V. Lobaskin, *Nanomaterials*, 2023, **13**, 1857.

96 H. Lopez and V. Lobaskin, *The Journal of Chemical Physics*, 2015, **143**, 243138.

97 H. Lopez, E. G. Brandt, A. Mirzoev, D. Zhurkin, A. Lyubartsev and V. Lobaskin, *Advances in Experimental Medicine and Biology*, Springer International Publishing, 2017, pp. 173–206.

98 S. A. Alsharif, D. Power, I. Rouse and V. Lobaskin, *Nanomaterials*, 2020, **10**, 1967.

99 I. Rouse and V. Lobaskin, *Faraday Discuss.*, 2023, –.

100 J. N. Israelachvili, *The Handbook of Surface Imaging and Visualization*, CRC Press, 2022, pp. 793–816.

101 I. Rouse, D. Power, E. G. Brandt, M. Schneemilch, K. Kotsis, N. Quirke, A. P. Lyubartsev and V. Lobaskin, *Phys. Chem. Chem. Phys.*, 2021, **23**, 13473–13482.

102 B. Kharazian, N. Hadipour and M. Ejtehadi, *The international journal of biochemistry & cell biology*, 2016, **75**, 162–174.

103 K. Nienhaus and G. U. Nienhaus, *Small*, 2023, **19**, 2301663.

104 V. Karunakaran Annapoorani, S. Dutta, O. Ajia, O. A. Petrisor, V. Lobaskin and N.-V. Buchete, *The Journal of Physical Chemistry Letters*, 2025, **16**, 11356–11364.

105 H. Pan, M. Qin, W. Meng, Y. Cao and W. Wang, *Langmuir*, 2012, **28**, 12779–12787.

106 A. F. Lima and A. A. Sousa, *Physchem*, 2023, **3**, 385–410.

107 H. Lee, *Small*, 2020, **16**, 1906598.

108 J. Talbot, X. Jin and N.-H. L. Wang, *Langmuir*, 1994, **10**, 1663–1666.

109 J. Talbot, G. Tarjus, P. Van Tassel and P. Viot, *Colloids and Surfaces A: Physicochemical and Engineering Aspects*, 2000, **165**, 287–324.

110 V. P. Zhdanov and N.-J. Cho, *Mathematical Biosciences*, 2016, **282**, 82–90.

111 P. Mosaddeghi Amini, I. Rouse, J. Subbotina and V. Lobaskin, *Beilstein J. Nanotechnol.*, 2024, **15**, 215–229.

112 M. v. Smoluchowski, *Zeitschrift für physikalische Chemie*, 1918, **92**, 129–168.

113 S. Tenzer, D. Docter, J. Kuharev, A. Musyanovych, V. Fetz, R. Hecht, F. Schlenk, D. Fischer, K. Kiouptsi, C. Reinhardt, K. Landfester, H. Schild, M. Maskos, S. Knauer and R. Stauber, *Nature nanotechnology*, 2013, **8 10**, 772–81.

114 P.-L. Latreille, J.-M. Rabanel, M. Le Goas, S. Salimi, J. Arlt, S. A. Patten, C. Ramassamy, P. Hildgen, V. A. Martinez and X. Banquy, *Advanced Materials*, 2022, **34**, 2203354.

115 S. M. Bhattacharjee, A. Giacometti and A. Maritan, *Journal of Physics: Condensed Matter*, 2013, **25**, 503101.

116 P. J. Flory, *Principles of Polymer Chemistry*, Cornell University Press, Ithaca, NY, 1953.

117 L. Ramirez, S. Ramseier Gentile, S. Zimmermann and S. Stoll, *Water*, 2019, **11**, 721.

118 A. Lappala, S. Mendiratta and E. M. Terentjev, *Macromolecules*, 2015, **48**, 1894–1900.

119 T. I. Morozova and A. Nikoubashman, *The Journal of Physical Chemistry B*, 2018, **122**, 2130–2137.

120 W.-L. Chen, R. Cordero, H. Tran and C. K. Ober, *Macromolecules*, 2017, **50**, 4089–4113.

121 T. Trumpour and J. A. Forrest, *The European Physical Journal E*, 2022, **45**, 85.

122 N. Hueppe, F. R. Wurm and K. Landfester, *Macromolecular Rapid Communications*, 2022, 2200611.

123 G.-B. Im, Y. G. Kim, I.-S. Jo, T. Y. Yoo, S.-W. Kim, H. S. Park, T. Hyeon, G.-R. Yi and S. H. Bhang, *Journal of Hazardous Materials*, 2022, **430**, 128411.

124 T. Du, X. Yu, S. Shao, T. Li, S. Xu and L. Wu, *Environmental Science & Technology*, 2023, **57**, 3206–3217.

125 S. Ducoli, S. Federici, R. Nicsanu, A. Zendrini, C. Marchesi, L. Paolini, A. Radeghieri, P. Bergese and L. E. Depero, *Environ. Sci.: Nano*, 2022, **9**, 1414–1426.

126 J. Gigault, H. El Hadri, B. Nguyen, B. Grassl, L. Rowenczyk, N. Tufenkji, S. Feng and M. Wiesner, *Nature Nanotechnology*, 2021, 1–7.

127 D. Choi, J. Hwang, J. Bang, S. Han, T. Kim, Y. Oh, Y. Hwang, J. Choi and J. Hong, *Science of The Total Environment*, 2021, **752**, 142242.

View Article Online
DOI: 10.1039/D5EN00784D

128 A. Schrade, V. Mailänder, S. Ritz, K. Landfester and U. Ziener, *Macromolecular Bioscience*, 2012, **12**, 1459–1471.

129 S. Lerch, M. Dass, A. Musyanovych, K. Landfester and V. Mailänder, *European Journal of Pharmaceutics and Biopharmaceutics*, 2013, **84**, 265–274.

130 H.-J. Butt, K. Graf and M. Kappl, *Physics and chemistry of interfaces*, John Wiley & Sons, 2023.

131 S. Mahanta, P. Vallejo-Ramirez, N. Karedla, P. Puczkarski and M. Krishnan, *Proceedings of the National Academy of Sciences*, 2022, **119**, e2209955119.

132 *United Atom/NPCoronaPredict software at GitHub*, 2024, `https://github.com/ucd-softmatterlab/NPCoronaPredict`.

133 S. Sugio, A. Kashima, S. Mochizuki, M. Noda and K. Kobayashi, *Protein Engineering, Design and Selection*, 1999, **12**, 439–446.

134 J. M. Kollman, L. Pandi, M. R. Sawaya, M. Riley and R. F. Doolittle, *Biochemistry*, 2009, **48**, 3877–3886.

135 E. O. Saphire, P. W. H. I. Parren, R. Pantophlet, M. B. Zwick, G. M. Morris, P. M. Rudd, R. A. Dwek, R. L. Stanfield, D. R. Burton and I. A. Wilson, *Science*, 2001, **293**, 1155–1159.

136 B. J. Janssen, E. G. Huizinga, H. C. Raaijmakers, A. Roos, M. R. Daha, K. Nilsson-Ekdahl, B. Nilsson and P. Gros, *Nature 2005 437:7058*, 2005, **437**, 505–511.

137 Z. Wu, V. Gogonea, X. Lee, M. A. Wagner, X.-M. Li, Y. Huang, A. Undurti, R. P. May, M. Haertlein, M. Moulin, I. Gutsche, G. Zaccai, J. A. DiDonato and S. L. Hazen, *Journal of Biological Chemistry*, 2009, **284**, 36605–36619.

138 S. Jo, X. Cheng, J. Lee, S. Kim, S.-J. Park, D. S. Patel, A. H. Beaven, K. I. Lee, H. Rui, S. Park *et al.*, *Journal of computational chemistry*, 2017, **38**, 1114–1124.

139 M. H. Olsson, C. R. Søndergaard, M. Rostkowski and J. H. Jensen, *Journal of Chemical Theory and Computation*, 2011, **7**, 525–537.

140 V. Mishra and R. J. Heath, *International journal of molecular sciences*, 2021, **22**, 8411.

141 A. Sahu and J. D. Lambris, *Immunological reviews*, 2001, **180**, 35–48.

142 X. Yu, F. Hu, Q. Yao, C. Li, H. Zhang and Y. Xue, *BMC cancer*, 2016, **16**, 1–12.

143 J. B. Karlin, D. J. Juhn, J. Starr, A. M. Scanu and A. H. Rubenstein, *Journal of lipid research*, 1976, **17**, 30–37.

144 A. Leino, O. Impivaara, M. Kaitsaari and J. Järvisalo, *Clinical chemistry*, 1995, **41**, 1633–1636.

145 M. H. Jazayeri, A. A. Pourfathollah, M. J. Rasaee, Z. Porpak and M. E. Jafari, *Biomedicine & Aging Pathology*, 2013, **3**, 241–245.

146 M. J. Sippl, M. Ortner, M. Jaritz, P. Lackner and H. Flöckner, *Folding and Design*, 1996, **1**, 289–298.

147 S. Pronk, S. Páll, R. Schulz, P. Larsson, P. Bjelkmar, R. Apostolov, M. R. Shirts, J. C. Smith, P. M. Kasson, D. van der Spoel, B. Hess and E. Lindahl, *Bioinformatics*, 2013, **29**, 845–854.

148 J. Huang, S. Rauscher, G. Nawrocki, T. Ran, M. Feig, B. L. de Groot, H. Grubmüller and A. D. MacKerell, *Nature Methods*, 2016, **14**, 71–73.

149 J. Subbotina, P. D. Kolokathis, A. Tsoumanis, N. K. Sidiropoulos, I. Rouse, I. Lynch, V. Lobaskin and A. Afantitis, *Journal of Chemical Information and Modeling*, 2025, **65**, 3142–3153.

150 N. Ganji and G. D. Bothun, *Environmental Science: Nano*, 2021, **8**, 160–173.

151 U. Janke, N. Geist, E. Weilbeer, W. Levin and M. Delcea, *ChemBioChem*, 2024, e202400188.

152 D. Rajendran and N. Chandrasekaran, *ACS omega*, 2023, **8**, 43719–43731.

153 J. Shi, F. Tian, J. Lyu and M. Yang, *Journal of materials chemistry B*, 2015, **3**, 6989–7005.

154 J. Ghuman, P. Zunszain, I. Petitpas, A. A. Bhattacharya, M. Otagiri and S. Curry, *Journal of molecular biology*, 2005, **353 1**, 38–52.

155 B. J. Janssen, E. G. Huizinga, H. C. Raaijmakers, A. Roos, M. R. Daha, K. Nilsson-Ekdahl, B. Nilsson and P. Gros, *Nature*, 2005, **437**, 505–511.

156 P. Gros, F. J. Milder and B. J. Janssen, *Nature Reviews Immunology*, 2008, **8**, 48–58.

157 Z. Chen, M. Wang, W. Duan, Y. Xia, H. Liu and F. Qian, *Journal of Biological Chemistry*, 2025, **301**, 108250.

158 B. V. Geisbrecht, J. D. Lambris and P. Gros, Seminars in immunology, 2022, p. 101627.

159 B. Wang, X. Zhong, L. Fields, H. Lu, Z. Zhu and L. Li, *Journal of the American Society for Mass Spectrometry*, 2023, **34**, 459–471.

160 Y. Arima, M. Toda and H. Iwata, *Advanced drug delivery reviews*, 2011, **63**, 988–999.

161 H. Pedersen, R. K. Jensen, J. M. B. Jensen, R. Fox, D. V. Pedersen, H. G. Olesen, A. G. Hansen, D. Christiansen, S. M. Mazarakis, N. Lojek *et al.*, *The Journal of Immunology*, 2020, **205**, 2287–2300.

162 B. J. Janssen, E. F. Halff, J. D. Lambris and P. Gros, *Journal of Biological Chemistry*, 2007, **282**, 29241–29247.

163 C. Lamers, D. C. Mastellos, D. Ricklin and J. D. Lambris, *Trends in pharmacological sciences*, 2022, **43**, 629–640.

164 T. E. Mollnes, B. S. Storm, O. L. Brekke, P. H. Nilsson and J. D. Lambris, Seminars in Immunology, 2022, p. 101604.

165 S. M. Moghimi, A. J. Andersen, D. Ahmadvand, P. P. Wibroe, T. L. Andresen and A. C. Hunter, *Advanced drug delivery reviews*, 2011, **63**, 1000–1007.

166 A. J. Pinto, A. Chouquet, I. Bally, V. Rossi, N. M. Thielens, C. Dumestre-Pérard, R. Kunert, C. Gaboriaud, W. L. Ling and J.-B. Reiser, *The FEBS Journal*, 2025.

167 M. Tonigold, J. Simon, D. Estupiñán, M. Kokkinopoulou, J. Reinholz, U. Kintzel, A. Kaltbeitzel, P. Renz, M. P. Domogalla, K. Steinbrink *et al.*, *Nature nanotechnology*, 2018, **13**, 862–869.

168 N. Javkhlantugs, H. Bayar, C. Ganzorig and K. Ueda, *International Journal of Nanomedicine*, 2013, 2487–2496.

169 J. Wang, X. Chen, M. L. Clarke and Z. Chen, *The Journal of*

View Article Online
DOI: 10.1039/D5EN00784D

Physical Chemistry B, 2006, **110**, 5017–5024.

170 T. Lu and Z. Chen, *The journal of physical chemistry letters*, 2023, 3139–3145.

171 J. Gao, P. Stengel, T. Lu, Y. Wu, D. D. Hawker, K. E. Gutowski, J. M. Hankett, M. Kellermeier and Z. Chen, *Langmuir*, 2023, **39**, 12270–12282.

172 S. Köhler, F. Schmid and G. Settanni, *Langmuir*, 2015, **31**, 13180–13190.

173 A. Bratek-Skicki, P. Żeliszewska and Z. Adamczyk, *Colloids and Surfaces B: Biointerfaces*, 2013, **103**, 482–488.

174 H. Derakhshankhah, A. Hosseini, F. Taghavi, S. Jafari, A. Lotfabadi, M. R. Ejtehadi, S. Shahbazi, A. Fattahi, A. Ghasemi, E. Barzegari *et al.*, *Scientific reports*, 2019, **9**, 1558.

175 G. Dežecalić, N. Deželić and Ž. Telišman, *European Journal of Biochemistry*, 1971, **23**, 575–581.

176 S. McColman, R. Li, S. Osman, A. Bishop, K. P. Wilkie and D. T. Cramb, *Nanoscale*, 2021, **13**, 20550–20563.

177 D. Prozeller, C. Rosenauer, S. Morsbach and K. Landfester, *Biointerphases*, 2020, **15**, year.

178 R. Cukalevski, M. Lundqvist, C. Oslakovic, B. Dahlbäck, S. Linse and T. Cedervall, *Langmuir : the ACS journal of surfaces and colloids*, 2011, **27 23**, 14360–9.

179 X. Wang, J. Zhao, S. Ding and H. Zhang, *International Journal of Biological Macromolecules*, 2023, **238**, 124049.

180 M. M. Gruber, B. Hirschmugl, N. Berger, M. Holter, S. Radulović, G. Leitinger, L. Liesinger, A. Berghold, E. Roblegg, R. Birner-Gruenberger *et al.*, *Journal of nanobiotechnology*, 2020, **18**, 1–14.

181 M. N. Alemie, R. Bright, N. H. Nguyen, V. K. Truong, D. Palms, J. D. Hayball and K. Vasilev, *ACS Applied Materials & Interfaces*, 2024.

182 S. Köhler, F. Schmid and G. Settanni, *PLoS computational biology*, 2015, **11**, e1004346.

183 Z. J. Deng, M. Liang, I. Toth, M. J. Monteiro and R. F. Minchin, *ACS nano*, 2012, **6**, 8962–8969.

184 S. Yu, M. Shen, S. Li, Y. Fu, D. Zhang, H. Liu and J. Liu, *Environmental Pollution*, 2019, **255**, 113302.

185 M. Auguste, T. Balbi, A. Miglioli, S. Alberti, S. Prandi, R. Narizzano, A. Salis, G. Damonte and L. Canesi, *Nanomaterials*, 2021, **11**, 3291.

186 S. Panico, S. Capolla, S. Bozzer, G. Toffoli, M. D. Bo and P. Macor, *Pharmaceutics*, 2022, **14**, year.

187 V. Vu, G. B. Gifford, F. Chen, H. Benasutti, G. Wang, E. Groman, R. Scheinman, L. Saba, S. Moghimi and D. Simberg, *Nature nanotechnology*, 2018, **14**, 260 – 268.

188 A. Sellborn, M. Andersson, J. Hedlund, J. Andersson, M. Berglin and H. Elwing, *Molecular immunology*, 2005, **42 5**, 569–74.

189 T. Mészáros, G. T. Kozma, T. Shimizu, K. Miyahara, K. Turjeman, T. Ishida, Y. Barenholz, R. Urbanics and J. Szebeni, *International journal of nanomedicine*, 2018, **13**, 6345–6357.

190 M. Noris and G. Remuzzi, *Seminars in Nephrology*, 2013, **33**, 479–492.

191 N. S. Merle, S. E. Church, V. Fremeaux-Bacchi and L. T. Roumenina, *Frontiers in Immunology*, 2015, **6**, year.

192 R. Franzin, A. Stasi, M. Fiorentino, G. Stallone, V. Cantaluppi, L. Gesualdo and G. Castellano, *Frontiers in immunology*, 2020, **11**, 734.

193 D. Perez Sierra, A. Tripathi and A. Pillai, *Biomarkers in Neuropsychiatry*, 2022, **7**, 100056.

194 O. Fatoba, T. Itokazu and T. Yamashita, *The FEBS Journal*, 2022, **289**, 2085–2109.

195 F. Chen, G. Wang, J. I. Griffin, B. Brenneman, N. K. Banda, V. M. Holers, D. S. Backos, L. Wu, S. M. Moghimi and D. Simberg, *Nature Nanotechnology 2016 12:4*, 2016, **12**, 387–393.

196 S. Moghimi and T. Andresen, *Molecular Immunology*, 2009, **46**, 1571–1572.

197 R. Cornelius, J. Archambault and J. Brash, *Biomaterials*, 2002, **23 17**, 3583–7.

198 R. Cornelius, J. Macri and J. Brash, *Journal of biomedical materials research. Part A*, 2011, **99 1**, 109–15.

199 R. Cornelius, J. Macri, K. Cornelius and J. Brash, *Langmuir : the ACS journal of surfaces and colloids*, 2015, **31 44**, 12087–95.

200 X. Liu, W. Wei, Z. Liu, E. Song, J. Lou, L. Feng, R. Huang, C. Chen, P. C. Ke and Y. Song, *Proceedings of the National Academy of Sciences*, 2021, **118**, e2108131118.

201 L. Treuel, S. Brandholt, P. Maffre, S. Wiegele, L. Shang and G. Nienhaus, *ACS nano*, 2014, **8 1**, 503–13.

202 K. Yamasaki, V. T. G. Chuang, T. Maruyama and M. Otagiri, *Biochimica et Biophysica Acta (BBA)-General Subjects*, 2013, **1830**, 5435–5443.

203 N. H. Moghadam, S. Salehzadeh, J. Rakhtshah, A. H. Moghadam, H. Tanzadehpanah and M. Saidijam, *International journal of biological macromolecules*, 2019, **125**, 931–940.

204 X. Zhang, B. Niebuur, P. Chytil, T. Etrych, S. K. Filippov, A. Kikhney, D. C. F. Wieland, D. Svergun and C. Papadakis, *Biomacromolecules*, 2018, **19 2**, 470–480.

205 F. Yang, Y. Zhang and H. Liang, *International Journal of Molecular Sciences*, 2014, **15**, 3580 – 3595.

206 Z. Zhivkova, *Current pharmaceutical design*, 2015, **21 14**, 1817–30.

207 Z. Sunil, J. Thomas, M. Shivashankar and N. Chandrasekaran, *Environmental Science: Nano*, 2024, **11**, 1012–1022.

208 P. Daneshgar, A. A. Moosavi-Movahedi, P. Norouzi, M. R. Ganjali, A. Madadkar-Sobhani and A. A. Saboury, *International Journal of Biological Macromolecules*, 2009, **45**, 129–134.

209 L. J. Juang, W. S. Hur, L. M. Silva, A. W. Strilchuk, B. J. Francisco, J. Leung, M. K. Robertson, D. Groeneveld, B. L. Prairie, E. M. Chun, A. Cap, J. Luyendyk, J. Palumbo, P. Cullis, T. Bugge, M. Flick and C. Kastrup, *Blood*, 2021.

210 Z. J. Deng, M. Liang, M. Monteiro, I. Toth and R. F. Minchin, *Nature nanotechnology*, 2011, **6**, 39–44.

211 J. Liu, Y. Ma, D. Zhu, T. Xia, Y. Qi, Y. Yao, X. Guo, R. Ji and W. Chen, *Environmental science & technology*, 2018, **52 5**,

View Article Online
DOI: 10.1039/D5EN00784D

2677–2685.
212 X. Li, E. He, K. Jiang, W. Peijnenburg and H. Qiu, *Water research*, 2020, **190**, 116742.
213 Z. Dong, Y. Hou, W. Han, M. Liu, J. Wang and Y. Qiu, *Water research*, 2020, **182**, 115978.
214 S. Kihara, N. J. van der Heijden, C. Seal, J. Mata, A. Whitten, I. Köper and D. McGillivray, *Bioconjugate chemistry*, 2019, **30 4**, 1067–1076.
215 R. Cukalevski, S. A. Ferreira, C. Dunning, T. Berggård and T. Cedervall, *Nano Research*, 2015, **8**, 2733–2743.
216 M. Kendall, P. Ding and K. Kendall, *Nanotoxicology*, 2011, **5**, 55 – 65.

View Article Online
DOI: 10.1039/D5EN00784D

Journal Name

ARTICLE TYPE

Cite this: DOI: 00.0000/xxxxxxxxxx

Modelling bionano interactions and potential health risks for environmental nanoplastics: the case of functionalized polystyrene.†

Julia Subbotina,*[1] Oran McElligott,[a] and Vladimir Lobaskin[a]

1 Data availability Statement

Additional data is available from Supporting Information online: LINK. The PDF file contains a visualisation of the PS NPs multiscale models used in the work, a visualization of the lowest energy complexes corresponding to minima found at the adsorption heatmaps; tables for multiple adsorption poses of protein-NP complexes and corresponding AAs, nearest to the NP's surface. The PDB structures of predicted complexes (lowest energies) and the Jupiter Notebook for their visualization, PS potentials, and UA configurational files are available via GitHub link: https://github.com/juliasubbotina/uaCoronaPS. The latest official release of UA/NPCoronaPredict package (including material parameters, examples of required files, and postprocessing tools) can be found here: https://github.com/ucdsoftmatterlab/NPCoronaPredict .

[1] School of Physics, College of Science, University College Dublin, Dublin, Ireland. Email: yulia.subbotina@ucd.ie